NUMERICAL MODELING AND SIMULATION OF MATERIAL REMOVAL IN LASER DRILLING OF THIN METAL SHEETS USING MESHFREE COLLOCATION METHODS

DIAA ABDELMONEM MAHMOUD ABIDOU

FACULTY OF ENGINEERING
UNIVERSITY OF MALAYA
KUALA LUMPUR

2017

NUMERICAL MODELING AND SIMULATION OF MATERIAL REMOVAL IN LASER DRILLING OF THIN METAL SHEETS USING MESHFREE COLLOCATION METHODS

DIAA ABDELMONEM MAHMOUD ABIDOU

THESIS SUBMITTED IN FULFILLMENT OF THE REQUIREMENTS FOR THE DEGREE OF DOCTOR OF PHILOSOPHY

FACULTY OF ENGINEERING
UNIVERSITY OF MALAYA
KUALA LUMPUR

2017

UNIVERSITI MALAYA

ORIGINAL LITERARY WORK DECLARATION

Name of Candidate: **Diaa Abdelmonem Mahmoud Abidou**

Registration/Matric No.: **KHA130144**

Name of Degree: **Doctor of Philosophy**

Title of Project Paper/Research Report/Dissertation/Thesis ("this Work"):

Numerical Modeling and Simulation of Material Removal in Laser Drilling of Thin Metal Sheets Using Meshfree Collocation Methods

Field of Study: **Meshfree Numerical Simulation**

I do solemnly and sincerely declare that:

(1) I am the sole author/writer of this Work;
(2) This Work is original;
(3) Any use of any work in which copyright exists was done by way of fair dealing and for permitted purposes and any excerpt or extract from, or reference to or reproduction of any copyright work has been disclosed expressly and sufficiently and the title of the Work and its authorship have been acknowledged in this Work;
(4) I do not have any actual knowledge nor do I ought reasonably to know that the making of this work constitutes an infringement of any copyright work;
(5) I hereby assign all and every rights in the copyright to this Work to the University of Malaya ("UM"), who henceforth shall be owner of the copyright in this Work and that any reproduction or use in any form or by any means whatsoever is prohibited without the written consent of UM having been first had and obtained;
(6) I am fully aware that if in the course of making this Work I have infringed any copyright whether intentionally or otherwise, I may be subject to legal action or any other action as may be determined by UM.

Candidate's Signature Date

Subscribed and solemnly declared before,

Witness's Signature Date

Name:
Designation:

ABSTRACT

A simplified lightweight numerical model is proposed for predicting the hole geometry in laser drilling of thin metal sheets. A 2D axisymmetric model for transient metal laser drilling is adopted, and three different meshfree collocation methods are employed and compared with each other in terms of computational efficiency and results accuracy. Collocation discretization (i.e. strong-form) of meshless local Petrov-Galerkin (MLPG), symmetric smoothed particle hydrodynamics (SSPH) and radial point interpolation method (RPIM) is used to harness its advantages of significant reduction in computational time and constructing global matrices in a straightforward manner over their weak-form. The 2D domain is discretized into a finite number of particels, then shape functions of the neighbors are obtained. Laser beam is assumed to be continuous wave with Gaussian distribution, while particles are assumed to be removed upon reaching the melting temperature under the effect of a highly pressurized assist gas. MATLAB code is constructed for numerical simulation, and results are compared with previously published relevant work. A good agreement is shown for each method with little deviation of hole geometry prediction from each other. SSPH is chosen as the best method for the proposed work since it is significantly superior to MLPG and RPIM in terms of CPU time. Despite considering a fixed value for laser absorptivity, the proposed numerical model is shown to be computationally efficient and accurate standalone platform for predicting the penetration depth of laser drilling of thin metal sheets. The computational efficiency of meshfree collocation methods is exploited to build a lightweight standalone application with graphical user interface (GUI). This application has the potential of integrating the present model into the front panel of typical laser processing machines in order to provide an estimation of the keyhole geometry for arbitrarily given process parameters and target metals, which saves unnecessarily time-consuming and costly experimentation.

ABSTRAK

Suatu Model Berangka Ringan Dipermudahkan telah dicadangkan untuk meramalkan geometri lubang dalam penggerudian laser bagi kepingan logam nipis. Suatu model simetri sepaksi 2D untuk penggerudian laser logam transien diguna pakai dan tiga kaedah bebas-mesh kolokasi (penempatan bersama) berbeza digunakan dan dibandingkan antara satu sama lain dari segi pengiraan kecekapan dan ketepatan keputusan. Kolokasi pendiskretan (iaitu bentuk-kuat) daripada Petrov-Galerkin (MLPG) tempatan tanpa-mesh, hidrodinamik zarah simetri terlicin (SSPH) dan jejarian kaedah titik interpolasi (RPIM) telah digunakan. Kolokasian pendiskretan mempunyai kelebihan pengurangan ketara dalam masa pengiraan komputesional dan membina matriks global dengan cara yang terus-mudah berbanding bentuk yang lemah. Domain 2D didiskretankan ke dalam beberapa zarah terhingga, maka bentuk fungsi jiran boleh diperolehi. Pancaran laser dianggap sebagai gelombang berterusan dengan taburan Gaussian, manakala zarah diandaikan akan dikeluarkan apabila mencapai takat suhu lebur di bawah kesan gas bantuan bertekanan tinggi. Kod MATLAB dibina untuk simulasi berangka dan keputusannya dibandingkan dengan kerja-kerja berkaitan yang pernah diterbitkan sebelum ini. Satu keputusan yang sama bandingan ditunjukkan bagi setiap kaedah dengan sedikit selisihan ramalan lubang geometri daripada satu sama lain. SSPH dipilih sebagai kaedah terbaik untuk kerja yang dicadangkan kerana ia adalah lebih baik daripada MLPG dan RPIM dari segi masa CPU. Walaupun mempertimbangkan nilai tetap untuk keboleh-serapan laser, model berangka yang ditunjukkan sebagai platfom tersendiri adalah cekap-komputeran dan tepat untuk meramalkan kedalaman penembusan penggerudian laser bagi kepingan logam nipis. Untuk kaedah kolokasian bebas-mesh, kelebihan mereka untuk mengendalikan apa-apa masalah pemisahan domain dengan beban pengiraan minimum boleh dieksploitasi untuk membina aplikasi yang berdiri sendiri lengkap dengan GUI. Aplikasi ini mempunyai potensi untuk mengintegrasikan model sedia ada ke dalam panel hadapan mesin pemprosesan laser biasa untuk menyediakan anggaran geometri lubang-kunci untuk

anggar-wenang parameter proses yang diberi dan logam sasaran.

ACKNOWLEDGMENTS

First and foremost, praises and thanks to Allah, the Almighty, for giving me the strength, knowledge and opportunity to undertake this research study and satisfactorily complete it. Without his blessings, I couldn't have achieved anything.

I must thank Allah for my mother who hasn't stopped wishing me all the best every day and night. My wife support during my ups and downs will be forever appreciated and remembered.

Many thanks to my former supervisor Prof. Mohsen Hassan who believed in me to pursue this work and gave me the whole support I needed. Sincere thanks to my supervisors Prof. Nukman Bin Yusoff and Assoc. Prof. Nik Nazri for their immense support, motivation and backing me up when I started to get frustrated. Particular thanks go to Mr. Md. Abu Omar Bin Awang whose suggestions and guidance were indispensable to this work and the associated publications.

My greatest gratitude goes to Prof. Ahmed Sarhan who didn't hesitate for a moment to give me his time, effort and all kinds of unconditional support as if I was one of his students, although he hasn't officially been my supervisor. Particular thanks goes to his former student Amin Ezazi whose unconditional help and support during my experiments were pivotal. Also, I am highly appreciative of the great help given by Dr. Aoday Mohamad for his time and efforts he gave to make me able to finish my experimental work.

I am greatly grateful to Puan Zuriani and Eng. Asrul who unconditionally gave me all kinds of support for doing my experiments at SIRIM corporate.

Table of Contents

List of Figures

List of Tables

List of Symbols

C_p	[J kg^{-1} K^{-1}]	Specific heat
h	[μm]	Support domain radius
h_a	[W m^{-2} K^{-1}]	Coefficient of convective heat transfer
k	[W m^{-1} K^{-1}]	Coefficient of thermal conductivity
$\hat{n}_l$		Unit normal vector outward laser-irradiated surface
n		Number of neighboring particles inside the support domain
N		Total number of particles in the whole domain
P_l	[W]	Laser power
r_b	[μm]	Laser beam radius at the focal point
t	[μs]	Laser processing time
T	[K]	Particle temperature
T_a	[K]	Ambient temperature
T_m	[K]	Metal melting temperature
α_l		Laser absorptivity
Γ_l		Laser-irradiated boundary
Δ	[μm]	Nodal spacing

Δt	$[\mu s]$	Simulation time step
λ	$[m^2\,s^{-1}]$	Thermal diffusivity
ρ	$[kg\,m^{-3}]$	Density
Ω		Whole domain

List of Abbreviations

AMP	advanced machining process
CFD	computational fluid dynamics
CSM	computational solid mechanics
EFG	element-free Galerkin
FDM	finite difference method
FEM	finite element method
FPM	finite point method
FVM	finite volume method
GFDM	generalized finite difference method
GUI	graphical user interface
IFPM	isoparametric finite point method
LBM	laser beam machining
MLPG	meshless local Petrov-Galerkin
MLS	moving least square
MSPH	modified smoothed particle hydrodynamics
PDE	partial differential equation

RBF	radial basis function
RKPM	reproducing kernel particle method
RPIM	radial point interpolation method
SPH	smoothed particle hydrodynamics
SSPH	symmetric smoothed particle hydrodynamics
WLS	weighted least square

CHAPTER 1: INTRODUCTION

1.1 Background

Laser beam machining (LBM) is considered to be one of the advanced machining processs (AMPs). Due to its non-contact nature and microscale precision, LBM has become vital to fulfill the strict requirements of final products size, material, operating conditions, etc. For industrial lasers, considering the physical nature of the active medium, there are gas and solid state lasers. Moreover, laser drilling can be done in different approaches such as single pulse, percussion and trepanning. Analytical modelling and numerical simulation help further understand the effect of process parameters, melt expulsion, molten pool hydrodynamics and reflectivity/absorptivity. For laser drilling, analytical modeling and numerical simulation have been pursued to help in predicting the molten metal flow field, hole geometry and material removal rate in addition to understanding the effects of process parameters.

Grid or mesh-based numerical methods have been commonly used as an essential tool in solving problems in many fields of engineering and science such as computational fluid dynamics (CFD) and computational solid mechanics (CSM). Finite difference method (FDM) was heavily used for solving the governing partial differential equations for simple geometries. Moreover, finite volume method (FVM) and finite element method (FEM) succeeded in handling complex problems in both fields of fluid flow and solid mechanics. Generally speaking, mesh-based approach relies on discretizing the physical domain into finite number of elements with fixed number of nodes. Although mesh-based numerical methods are well developed tools for the analysis of advanced problem in both fluid and solid mechanics, there are some difficulties that limit their applicability in, for example, high deformation and free surface problems. Massive computational load and continuous re-meshing are associated with handling such problems, yet the results may not be accurate enough.

Consequently, the need for numerical approach to handle such problems with minimum computational load and accurate enough results has been rapidly investigated and pursued. Accordingly, meshfree methods have been introduced to handle such problems by discretizing the whole physical domain into finite number of particles instead of cells/nodes as in mesh-based methods. Each particle has both physical meaning and properties of mass, velocity, temp, etc. The solution at each particle can be approximated using a kernel function centered at the particle of interest. The kernel only allows a set of the particle neighbors lying within the prescribed kernel radius of support to contribute to the function value at the particle of interest.

1.2 Problem Statement

Since laser drilling is one of the most important AMPs, it is vital to understand the effect of the process multiple parameters at the lowest possible cost. Therefore, its numerical modeling and simulation aim to give insight into the output dependency on the process parameters. Conventional mesh-based methods are have limitations in handling such problems with severe deformation without massive computational load and numerous re-meshing as in, for example, metal laser processing. Therefore, meshfree methods will be addressed in this work of numerical simulation of metal laser drilling where they can handle domain deformation/separation in a more computationally efficient and easier way.

1.3 Scope of Study

This work aims to exploit the high potential of meshfree methods and apply them to the simulation of metal laser drilling to harness their advantages of handling problems of severe deformation and domain separation with minimum computational load. Furthermore, a standalone application is developed in order to show the expected output for a set of arbitrary input process parameters. Therefore, the application of meshfree methods to the numerical simulation of metal laser drilling results in a lightweight standalone application that can be seamlessly integrated inside the software of industrial laser machines.

1.4 Objective of Study

This study is going to:

- model and simulate the metal removal in laser drilling using different meshfree collocation methods in order to estimate the transient development of the laser-drilled hole shape and penetration time;
- validate the introduced numerical model against relevant published work and experimental data;
- provide a fully functional standalone application that masks the proposed model with a user-friendly graphical user interface (GUI).

1.5 Outline of the Thesis

This thesis is arranged into five main chapters as follows:

- In chapter 1, the research background, problem statement, study scope, objectives and methodology are introduced.
- In chapter 2, previous work in both areas of metal laser drilling and meshfree methods is reviewed where the mechanism of metal laser drilling is thoroughly given.
- In chapter 3, the methodology is deeply discussed, and the mathematical formulation of each meshfree method is thoroughly given. Additionally, the model assumptions are given in addition to its underlying fundamental logic.
- In chapter 4, the model results and their validation against the previous relevant work and the experimental data are comprehensively discussed.
- In chapter 5, the highlights of the present work are concluded, while future recommendations are given for further development of the introduced model.

CHAPTER 2: LITERATURE REVIEW

2.1 Introduction

Since the introduction of first working laser in 1960 (Maiman, 1960), LBM has proven to be one of the most important industrial processes. LBM has many advantages, including, but not limited to, the absence of tools wear, materials processing with up to nano-scale accuracy, drilling of high aspect ratio holes, feasible processing of wide range of materials and alloys, and the short processing time (Yeo, Tam, Jana, & Lau, 1994; Gower, 2000; Meijer, 2004; Ion, 2005; Dubey & Yadava, 2008; Schulz, Eppelt, & Poprawe, 2013). Because it is a physically complex process, a lot of effort has been devoted to develop analytical and numerical models of LBM to investigate and improve as accurately as possible. For instance, FDM and FEM in addition to analytical models were used/developed to construct numerical models to solve for the temperature distribution and kerf/hole geometry (Modest, 1996; Cheng, Tsui, & Clyne, 1998; Kim & Zhang, 2001; Kim, 2005; Kar, Rockstroh, & Mazumder, 1992; Ganesh, Bowley, Bellantone, & Hahn, 1996; Ganesh, Faghri, & Hahn, 1997b, 1997a). Additionally, thermal stresses are of great interest in LBM process since the rapid heating of the target material results in thermally nonuniform deformation which is the main cause of residual thermal stresses. Therefore, a plenty of numerical works quantitatively investigated such a phenomena (Paek & Gagliano, 1971; Li & Sheng, 1995; Yilbas & Naqvi, 2003; Akarapu, Li, & Segall, 2004; Arif, Yilbas, & Aleem, 2009; Harničárová et al., 2013; Veres, Berer, & Burgholzer, 2013).

Most of engineering problems have been numerically simulated using mesh-based numerical methods such as FEM, FDM and FVM. However, these mesh-based methods may fail in converging to an accurate solutions in problems of discontinuities, sever deformation and complex geometries because of the fixed topological connectivity between the grid elements (Nguyen, Rabczuk, Bordas, & Duflot, 2008; Hua Li, 2013). Consequently, continuous remeshing is indispensable to overcome such limitations,

which leads to unfavourable heavy computational load. Nevertheless, the solution may not be accurate enough, and it will degrade more in case of higher dimensionality, discontinuity or deformation. Therefore, meshfree methods have been developed to replace/be coupled with mesh-based methods for handling such engineering problems. Briefly speaking, the domain of interest, in meshfree methods, is discretiszed into a set of finite particles to solve for the field variable at them. Each particle is spatially and physically defined by carrying properties of mass, velocity, temperature, etc. The main advantage of meshfree methods is that no fixed geometrical connectivity is existent which helps in handling problems of severe deformation and domain separation. smoothed particle hydrodynamics (SPH) was the first and most popular meshfree method. It was mainly developed to solve astrophysics problems (Gingold & Monaghan, 1977), then it was used in fluid dynamics and solid mechanics ones (Monaghan, 2005). Later on, several meshfree methods have been thoroughly developed and pursued such as element-free Galerkin (EFG), reproducing kernel particle method (RKPM) and meshless local Petrov-Galerkin (MLPG) (Liu & Gu, 2005).

In the following sections, a thorough review is given on the numerical simulation of laser drilling in terms of hole geometry, melt expulsion and molten pool hydrodynamics. Additionally, the application of meshfree methods to laser drilling will be shed light on to show the previous work that has been done and the potential future work that can be pursued in this area.

2.2 Modeling and Simulation of Laser Drilling Process

A lot of work has been done in the area of modeling and simulation of laser drilling. In this section, an overview of the previous work will be given. In von Allmen, 1976, a numerical model was provided to estimate the drilling velocity of metal laser drilling while considering both rates of liquid expulsion and evaporation. The model didn't consider the change of laser absorptivity or reflectivity. For the given experiment, it was found that at low laser intensity, the drilling mechanism is a normal evaporation, and at certain high intensity, the recoil pressure was high enough to expel the molten material and abruptly

accelerate the drilling as depicted in Figure 2.1.

In Chan and Mazumder, 1987, a one-dimensional analytical model was constructed to understand the damage caused by the laser-material interaction. The model shows that the increase in laser energy results in reduction of liquid layer thickness and making the evaporation the dominant drilling mechanism, while the converse holds true. A two-dimensional axisymmetric model in Kar et al., 1992 was developed for material laser-induced removal. The model considered the multiple reflections against the hole walls and the shear stress-induced molten pool flow. It was shown that considering the multiple reflections leads to estimating of higher cavity depth, thinner recast layer and more cylindrical cavity. An effective absorptivity of fixed 85% value was presented to account for the abrupt increase in laser absorption when the liquid layer progresses.

In Patel and Brewster, 1991b, 1991a, a theoretical model was developed for gas assisted low power laser-metal interaction. The model was restricted to the low power laser drilling where the drilling mechanism was assumed to predominantly be the liquid expulsion. It was shown that the assist gas type affects the drilling time, while the higher assist gas pressure is, the longer drilling time becomes until reaching a critical pressure beyond which the pressure has no significant effect.

A novel mathematical 2D axisymmetric model was developed in Ganesh et al., 1996 while considering the molten pool hydrodynamics and material removal by expulsion and evaporation. The novelty of model came from treating the molten pool as a deformable free surface considering the impact of vapor gas dynamics on the temperature and pressure over the melt surface. Moreover, the modeling of melt resolidification was provided. While in Ganesh et al., 1997a, 1997b, the model in Ganesh et al., 1996 was improved to account for the change in thermo-physical properties with temperature. Additionally, the melting was considered to take place over a temperature range, and the latent heat of fusion wasn't neglected.

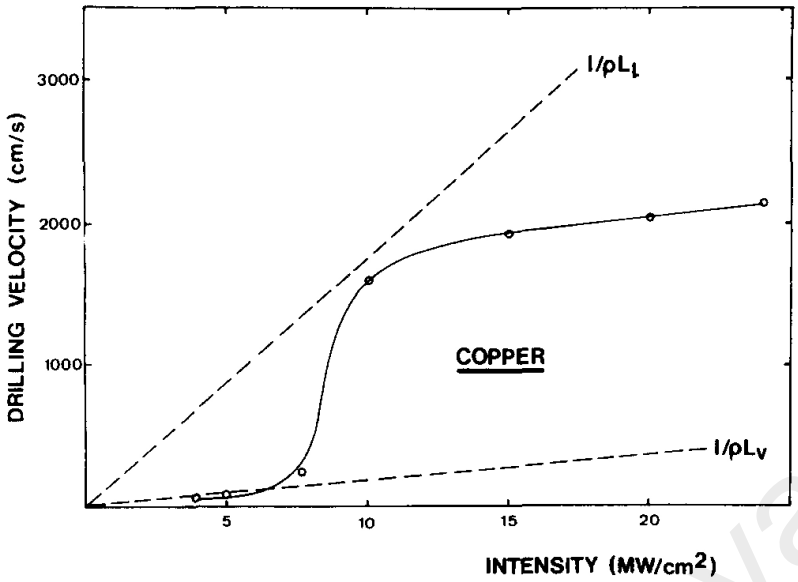

Figure 2.1: Measured drilling velocity (solid line) and both calculated fictitious drilling velocities (dashed lines) of pure evaporation $(1/\rho L_v)$ and pure liquefaction $(1/\rho L_l)$ (von Allmen, 1976)

In Solana, Kapadia, Dowden, and Marsden, 1999, an analytical modeling of laser drilling was given with consideration of laser attenuation due to its absorption by material vapor. The model showed good agreement with experimental work in the region of laser energy over which the liquid expulsion is the predominant mechanism. A thermal model of melting vaporization in laser drilling was developed in Zhang and Faghri, 1999. It was shown that the heat conduction losses to the solid material are small and have no significant effect on the vaporization. However, the melt front location is significantly affected by the heat conduction losses especially in case of low laser energy and long pulse time. A hydrodynamic physical model of laser material-interaction was developed in Semak, Damkroger, and Kempka, 1999 to simulate the temporal evolution of melt surface profile and estimate the temperature field. It was shown that the recoil pressure induces a significant convective heat transfer for absorbed laser intensities from 0.5 to 10 $\mathrm{MW\,cm^{-2}}$ which is the range of hydrodynamic drilling where the liquid expulsion is the main drilling mechanism.

An analytical one-dimensional model of laser drilling was derived in Shen, Zhang, Lu, and Ni, 2001. Temporal evolution of temperature was calculated before and after the occurrence of melting. A discontinuity in temperature gradient was found and attributed

to the latent heat of fusion. Additionally, materials with low thermal conductivity and high melting and boiling temperatures can be drilled faster than those with high thermal conductivity and low melting and boiling temperatures.

In Zhang, Yao, and Chen, 2001, an axisymmetric model was developed to track both solid-liquid and liquid-vapor interfaces. Additionally, discontinuities in Knudsen layer were considered. In this model, for high laser energy, a correction factor of plasma effect had to be applied to make the numerical results of hole depth and drilling efficiency have good agreement with experimental data since the plasma absorbs some incident laser energy and leads to lower energy irradiating the target material as shown in Figure 2.2. Plasma effect and vapor gas dynamics were shown to be significant at high incident laser energy.

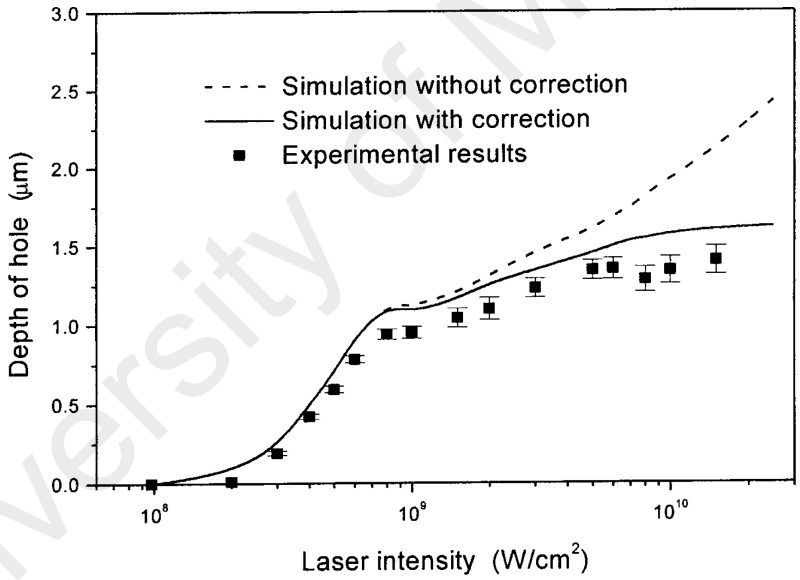

Figure 2.2: Effect of plasma correction factor where its application results in better agreement with the experimental data (Zhang, Yao, & Chen, 2001)

Two mathematical formulations in Verhoeven, Jansen, Mattheij, and Smith, 2003 were derived to solve for depth and temperature in laser-induced melting problem. One formulation employed Stefan condition, while the other used physical quantity enthalpy. The enthalpy method showed several advantages over the Stefan condition. In enthalpy method, the domain doesn't change with time so no tight restriction is imposed on the time step. Moreover, enthalpy method doesn't explicitly need the location of solid-liquid interface. Finally, enthalpy method is appropriate in case of alloys where the melting

takes place over a temperature range since the Stefan condition approach needs a distinct melting temperature.

In Ng, Crouse, and Li, 2006, a one-dimensional analytical model was developed based on that of Semak and Matsunawa, 1997; Low, Li, and Byrd, 2002. This model incorporated the oxidation effect of O_2 assist gas and took into consideration the effect of pulse width variation, while the recoil pressure formulation considered the hole variable depth. The model predicted, in good agreement with the experimental data, velocity of melt ejection, drilling velocity and the contributions of both melt ejection and evaporation to the overall drilling rate.

Pulsing mode of percussion laser drilling was investigated theoretically and experimentally in Salonitis, Stournaras, Tsoukantas, Stavropoulos, and Chryssolouris, 2007. The theoretical model considered only melting not vaporisation, which makes it suitable for addressing low to medium laser intensities. It was found the time needed for reaching the melting temperature is dependent on the pulsing frequency, and the maximum keyhole depth is independent of the pulsing frequency. In Harp, Dilwith, and Tu, 2008, fiber laser was investigated to find its feasibility of producing micro holes using microseconds pulses. Its performance was found to be as high as that of nanosecond laser in addition to holes with higher depth per pulse.

The work in Shidfar, Alinejadmofrad, and Garshasbi, 2009 introduced a conjugate gradient method (CGM)-based algorithm for predicting the melt depth. The laser processing was treated as an inverse heat conduction problem with unknown moving interface, and CGM was used to solve this inverse problem. In Collins and Gremaud, 2011, a simple axisymmetric mathematical model of laser drilling was introduced and reduced to one-dimensional after cross-sectional averaging. The model considered the regime of high laser fluence at which the evaporation is the main ablation mechanism, and the liquefaction played a secondary role. The model simulated the progress of solid-vapor interface while considering Knudsen layer discontinuities.

The model developed in Semak et al., 1999 was thoroughly investigated in Semak and Miller, 2013. The beam penetration was considered as melting through the target material or drilling through (due to evaporation and melt ejection). A wide range of laser pulse parameters (absorbed energy, pulse width, repetition rate and sample thickness) was studied to understand their effects for broad laser applications. The work in Zhang, Li, Chen, and Mazumder, 2013a gave a thorough experimental study of GG17 glass laser drilling. Additionally, a FEM model on ANSYS software was introduced. This study shed light on the effect of multiple reflections across keyhole walls and beam defocusing on the temporal evolution of the keyhole. Moreover, the drum-shaped profile of keyhole was examined in view of beam defocusing and reflections on the wall as depicted in Figure 2.3. This profile was attributed to the change of laser intensity with recessing keyhole front as shown in Figure 2.4.

In Zhang, Shen, and Ni, 2013b, 2014, a two-dimensional transient numerical model was established to simulate the long pulse (of order of milliseconds) laser drilling. The model considered the phase change of both melting and evaporation, gravity, recoil pressure and Marangoni effect, while a modified level-set method was employed to track the liquid-vapor interface. Laser pulse width and influence were investigated to understand their effects on the dynamic progress of keyhole and expelled melt. In order to better understand the laser drilling efficiency, an analytical and numerical study of laser drilling was provided in Pastras, Fysikopoulos, Stavropoulos, and Chryssolouris, 2014. The efficiency was defined as the ratio of removed volume to the energy consumed for removing this volume. It was shown that the efficiency increases with laser power and decreases with pulse duty and frequency. A theoretical model was developed in Yang, Chen, and Zhang, 2016 to understand the effect of melt flow on the material removal in laser drilling. It was found that its effect is dependent on the target material properties and may be ignored in some cases.

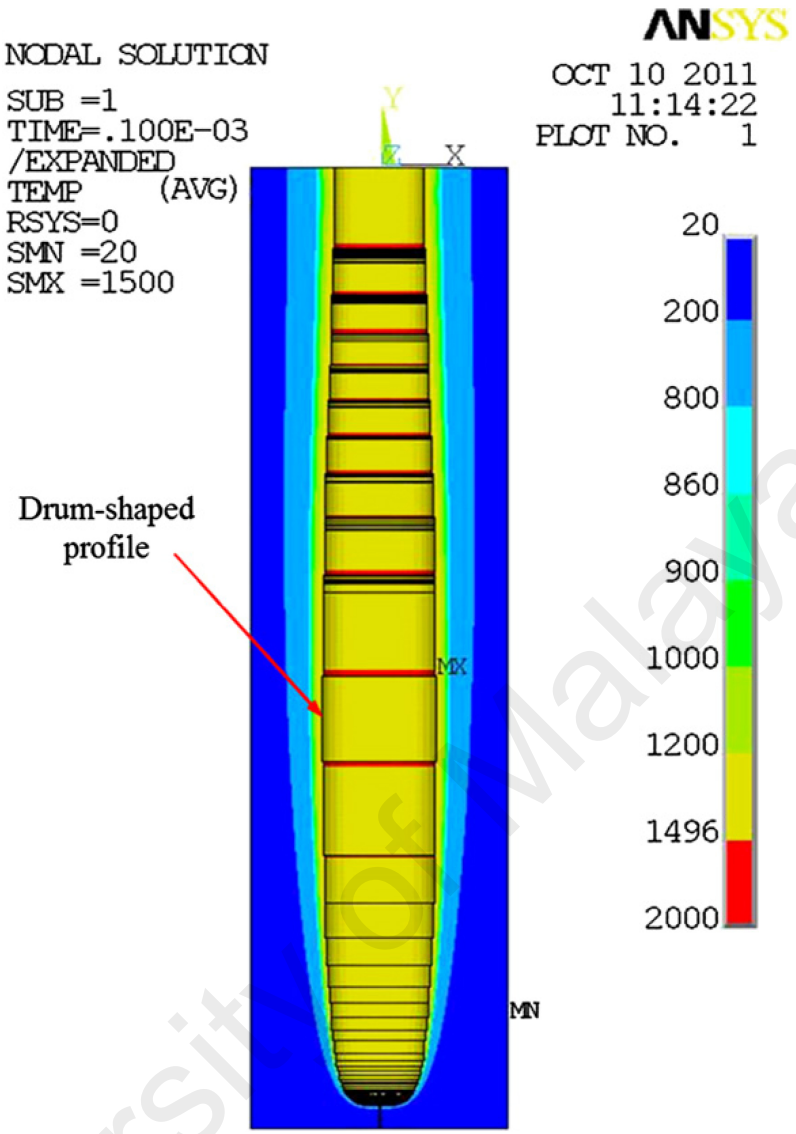

Figure 2.3: Simulation result shows a drum-shaped profile of the keyhole (Zhang, Li, Chen, & Mazumder, 2013a)

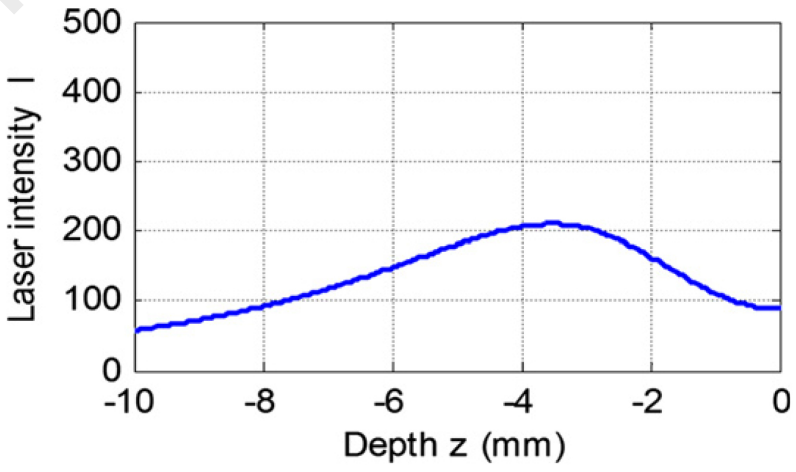

Figure 2.4: Variation of laser intensity with depth along a certain radial position ($x = 0.35$ mm) (Zhang, Li, Chen, & Mazumder, 2013a)

2.3 Meshfree Numerical Methods

2.3.1 Introduction to Meshfree Methods

Numerical simulation has been extensively used for solving problems in engineering and science. Grid- or mesh-based numerical methods have been commonly used as an essential tool in many fields such as CFD and CSM. FDM was heavily used for solving the governing partial differential equations for simple geometries. Moreover, FVM and FEM succeeded in handling complex problems in both fields of fluid flow and solid mechanics. Generally speaking, mesh-based approach relies on discretizing the physical domain into a finite number of elements/cells with fixed number of nodes. Although mesh-based numerical methods are well established tools for the analysis of advanced problem in both fluid and solid mechanics, there are some difficulties that limit their applicability in, for example, high deformation and free surface problems. Massive computational load and continuous re-meshing are associated with handling such problems, yet the results may not be accurate enough.

Consequently, the need for numerical approach to handle such problems with minimum computational load and accurate enough results has been rapidly investigated and pursued. Accordingly, since its introduction for astrophysics problems (Lucy, 1977; Gingold & Monaghan, 1977), meshfree methods have been introduced to handle such problems by discretizing the whole physical domain into finite number of particles, instead of cells/nodes as in mesh-based methods, as depicted in Figure 2.5. Each particle has both physical meaning and properties of mass, velocity, temp, etc. For example, in meshfree methods of local approximation, the solution at each particle can be approximated using a kernel/weight function centered at the particle of interest. The kernel function only allows a set of the particle neighbors lying within the prescribed kernel radius of support to contribute to the function value at the particle of interest (Li & Liu, 2002; Liu & Gu, 2005; Shaofan Li, 2007; Nguyen et al., 2008; Liu, 2009; Hua Li, 2013; Niraula, Han, & Wang, 2015).

Advantages of meshfree methods can be summarized as follows:

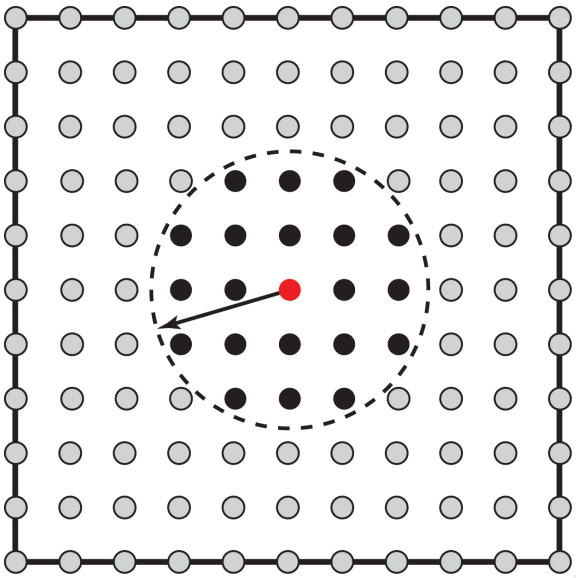

Figure 2.5: Meshfree discretization and the approximation field variable

1. Severe deformation can be easily handled without losing the accuracy as no fixed topological connectivity between the particles is existent.

2. Meshfree methods are favorable when dealing with material separation and discontinuities.

3. In certain domain area of interest, particles density can be increased for more accuracy as in h-adaptive methods.

4. Geometrically complex domains are easy to model without difficulties.

SPH is considered to be one of the first meshfree methods after its introduction in 1977. It was first developed for astrophysical problems (Lucy, 1977; Gingold & Monaghan, 1977; Rosswog, 2009; Springel, 2010), then, because of its potential to solve applied mechanics problems, it has been employed in solving different engineering problems. In other words, SPH has proven itself a potential numerical method for simulating problems of metal cutting and machining (Limido & Espinosa, 2006; Limido, Espinosa, Salaün, & Lacome, 2007; Espinosa et al., 2008; Su, Zhang, Hou, & Wang, 2008; Calamaz et al., 2009; Jianming, Na, & Wenjun, 2010; Limido et al., 2011; Zahedi, Li, Roy, Babitsky, & Silberschmidt, 2012),sloshing (Iglesias, Rojas, & Rodríguez, 2004; Souto-Iglesias, Delorme, Pérez-Rojas, & Abril-Pérez, 2006; Vorobyev, Kriventsev, & Maschek, 2011; Shao, Li, Liu, & Liu, 2012), dam break (Chang, Kao, Chang, & Hsu,

2011; Kao & Chang, 2012; Razavitoosi, Ayyoubzadeh, & Valizadeh, 2014), droplet deformation and splashing, (Zhang, Zhang, & Zheng, 2008; Xiong & Zhu, 2010) and multiphase fluid flow (Wang et al., 2016).

2.3.2 Classification of Meshfree Methods Formulation

In terms of formulation and discretization, meshfree methods can be categorized into global/local weak-form, combination of weak-form and collocation, and collocation methods. In global weak-form methods (e.g. EFG), a set of background cells are required to evaluate the integrals when using Galerkin weak-form over the global domain (Belytschko, Lu, & Gu, 1994). However, the need for background cells for global integration makes this kind of methods not truly meshfree ones. Therefore, to avoid using background cells, local weak-form methods were developed such as MLPG (Atluri & Zhu, 1998). In this kind of methods, the integration is evaluated locally over a quadrature domain which can be the same local domain where the test function is defined. Although they are computationally heavy and not easy to implement, weak-form methods are advantageous because of their high stability and accuracy especially in problems of derivative boundary conditions.

Employing Dirac delta as a test function, MLPG collocation method is produced where the difficult local integration is removed, thus the computational load is dramatically reduced (Atluri, 2004). Collocation or strong-form meshfree methods are based on direct discretization of the governing and boundary equations at the field nodes using some collocation techniques to form a set of discretized equations. The group of typical strong-form meshfree methods includes, but not limited to, SPH, generalized finite difference method (GFDM) (Liszka & Orkisz, 1980), finite point method (FPM) (Oñate, Idelsohn, Zienkiewicz, & Taylor, 1996) and collocation methods (Zhang, Song, Lu, & Liu, 2000). Strong-form meshfree methods has several advantages of easy implementation, computation efficiency and being truly meshfree methods without the need of background cells. Nevertheless, strong-form meshfree methods have limitations in their employment due to the inherent sensitivity of particles distributions and low

accuracy especially in problems of derivative boundary conditions.

2.3.3 Coupled Meshfree/Mesh-Based Methods

As previously said, meshfree methods are prominent computational tools when it comes to handling problems of severe deformation, complex geometries and domain separation. However, Meshfree methods are not the right choice when mild distortions are encountered since they are more computationally expensive than FEM. Therefore, FEMs are always of primary interest because of their high accuracy and less computational load in the absence of problems where extensive remeshing is needed. However, both advantages and disadvantages of meshfree and FEMs have drawn the attention of coupling between them. In such approach, the FEM can be employed at everywhere over the domain of interest, while its nodes are replaced by meshfree particles where FEM fails to converge. A lot of work has been done in this area and some of it can be found in Comas-Cardona, Groenenboom, Binetruy, and Krawczak, 2005; Fernández-Méndez, Bonet, and Huerta, 2005; Vuyst, Vignjevic, and Campbell, 2005; Rabczuk, Xiao, and Sauer, 2006; Campbell, Vignjevic, and Patel, 2008; Wang and Yang, 2009; Groenenboom, 2009; Zhang, Qiang, and Gao, 2011.

2.3.4 Meshfree Simulation of Laser Drilling

Since their introduction, meshfree methods have been rapidly gaining more attention towards engineering problems. However, their application in simulating laser drilling is still not quite enough. Because laser drilling is a thermal ablation process, careful attention should be paid towards the previous work in the area of solving heat transfer problems using meshfree methods to understand how they can be applied to such problems (Chen, Beraun, & Carney, 1999; Cleary & Monaghan, 1999; Jeong, Jhon, Halow, & van Osdol, 2003; Qian & Batra, 2004; Singh, 2004; Liu, Zhang, & Lu, 2005b; Singh, 2005; Wu & Tao, 2008; Zhang, Ouyang, & Zhang, 2009; Ahmadi, Sheikhy, Aghdam, & Nourazar, 2010; Dai, Wu, & Tao, 2011; Li, Chen, & Kou, 2011; Mugan, 2012; Fu, Chen, & Qin, 2012; Dai, Zheng, Liang, & Wang, 2013; Mirzaei & Schaback, 2013; Liang, Sun, Xi, & Liu, 2015; Zhang & Xiang, 2015). For laser drilling, up to the

author knowledge, few contributions have been introduced in this field.

In Muhammad, Rogers, and Li, 2013, an SPH-based platform (SPHysics) was used in simulating the laser drilling process of thin stainless steel coronary stent. The model considered hydrodynamics of the molten pool, penetration depth and ejection velocity of expelled particles in addition to the prediction of recast and spatter formation. On the other hand, in Kim, 2011, 2012, isoparametric finite point method (IFPM) was used in both strong and weak forms to simulate the metal laser drilling process. In this work, the laser drilling was simulated by finding the boundary shape that satisfied the heat balance through iterative scheme, however, the full-depth penetration wasn't clearly addressed using IFPM.

2.4 Conclusion

In summary, mesh-based numerical methods have been extensively employed and investigated in the area of numerical modeling and simulation of laser drilling process. However, after a thorough search of the relevant literature, meshfree methods seem to have not satisfactorily been investigated and employed as much as the mesh-based methods in this area despite their huge advantage of handling problems with severe deformations and domain separation, such as laser drilling, with less computational resources. This computational efficiency, for such problems, comes from the fact that meshfree methods discretize the domain into a finite number of particles without fixed topological connectivity between them, thus no computationally expensive remeshing is required as in case of mesh-based methods.

Therefore, this work novelty and main contribution is to construct a robust meshfree numerical model that can predict the transient keyhole geometry and penetration time for generic metal laser drilling. Accordingly, three widely-used meshfree collocation methods (MLPG, radial point interpolation method (RPIM) and symmetric smoothed particle hydrodynamics (SSPH)) will be employed in this work and compared to each other in terms of results accuracy and computational efficiency. In the next chapter, the

mathematical formulations of the present laser drilling model and aforementioned meshfree collocation methods will be rigorously given.

CHAPTER 3: METHODOLOGY

3.1 Introduction

In this chapter, laser drilling mechanism is explained, and its numerical model assumptions are comprehensively provided. Moreover, the mathematical formulations of MLPG, RPIM and SSPH are thoroughly given in detail in order to discretize the governing equation and its boundary conditions equations. MATLAB algorithm of the numerical model is explained, and its standalone application with GUI is introduced. Figure 3.1 shows the main steps taken, during this work, in the construction and validation of the present model.

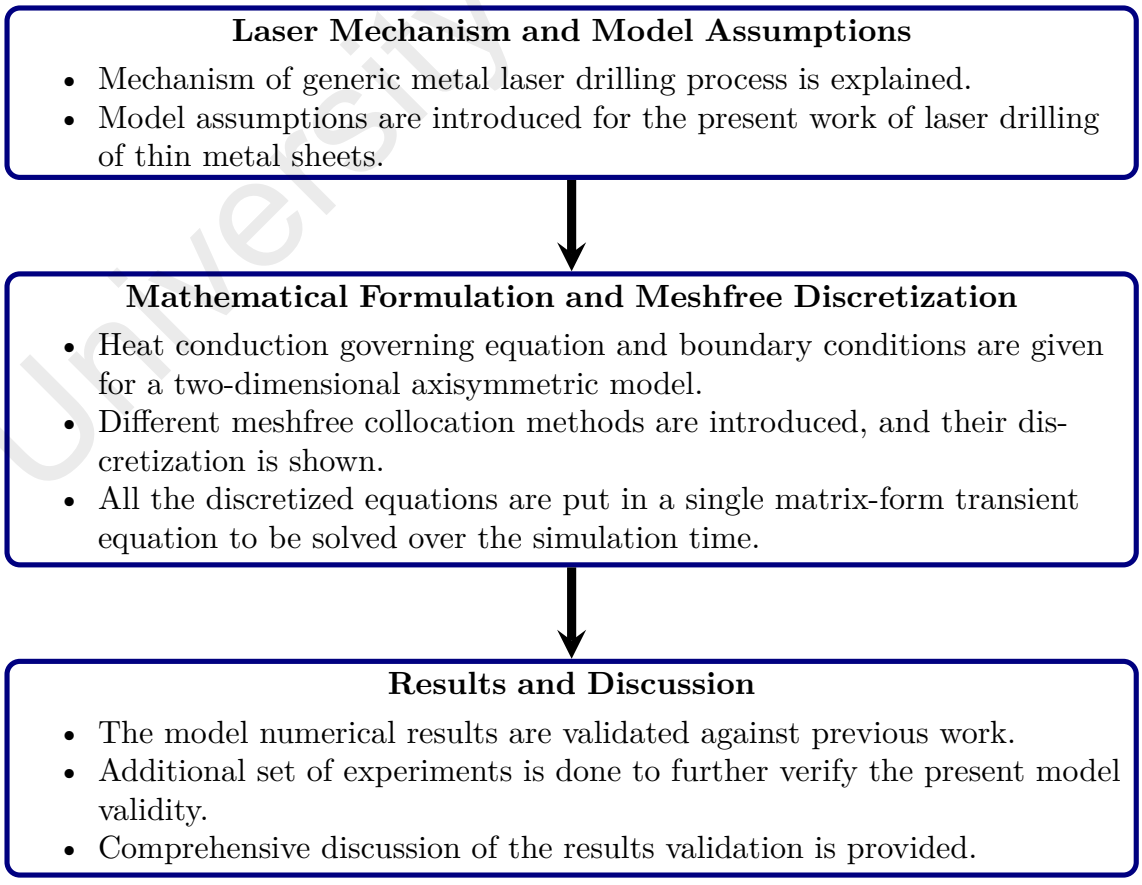

Figure 3.1: Flowchart of model construction and validation

3.2 Laser Drilling Mechanism and Mathematical Formulation

3.2.1 Mechanism of Metal Laser Drilling

Figure 3.2 shows the conventional metal laser drilling mechanism. In such a process, the metal is rapidly heated by the laser beam until reaching the melting temperature, while pressurized assist gas expels the molten metal away from he processed work-piece. Moreover, the assist gas protects the metal from the surrounding in addition to reducing the dross and recast.

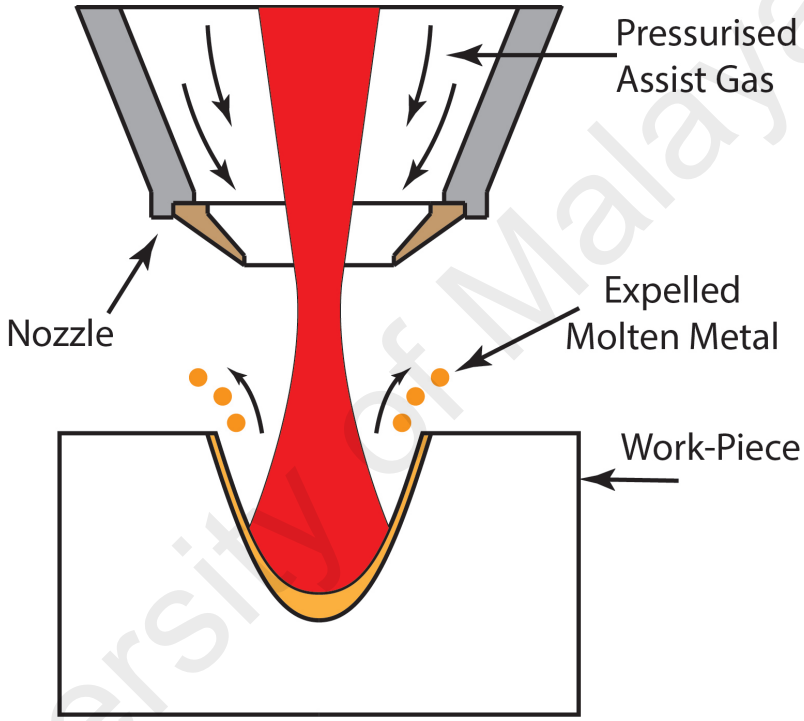

Figure 3.2: Mechanism of Fusion Laser Drilling

3.2.2 Assumptions of Numerical Model

During model construction, the following assumptions are considered:

1. Laser beam is continuous of Gaussian power distribution and vertically downward.
2. The radius of laser beam is constant and has value of the beam waist.
3. Laser irradiation is considered to be a surface heat flux not volumetric heat source.
4. The processed metal is isotropic with thermos-physical properties independent of temperature.

5. The molten metal does not show hydrodynamic behavior and is removed upon reaching the melting temperature.

6. Removed metal does not absorb the laser energy and is transparent.

7. Heat convection coefficient has single value for both convection and radiation losses.

3.2.3 Mathematical Formulation of Laser Drilling

Following the previous assumptions, the governing equation is the conventional heat conduction equation with Robin boundary conditions. For uniform Gaussian distribution of laser intensity, 2D axisymmetric model in cylindrical coordinates is considered. As a result, the governing equation of transient heat conduction for field particles is written as

$$\rho\, C_p \frac{\partial T}{\partial t} = k\left(\frac{1}{r}\frac{\partial T}{\partial r} + \frac{\partial T^2}{\partial r^2} + \frac{\partial T^2}{\partial z^2}\right) \quad \text{in} \quad \Omega. \tag{3.1}$$

with boundary conditions

$$\begin{aligned} k\frac{\partial T}{\partial n_l} &= q_l\, n_z + h_a\,(T_a - T) && \text{on } \Gamma_l, \\ k\frac{\partial T}{\partial r} &= h_a\,(T_a - T) && \text{on } r = l_r, \\ -k\frac{\partial T}{\partial z} &= h_a\,(T_a - T) && \text{on } z = 0, \\ \frac{\partial T}{\partial r} &= 0 && \text{on } r = 0. \end{aligned} \tag{3.2}$$

where $q_l = \frac{\alpha_l P_l}{\pi {r_b}^2} e^{-2\left(\frac{r}{r_b}\right)^2}$ is the absorbed laser heat flux.

Figure 3.3 depicts the domain governing equation with its Robin boundary conditions for the present problem, while Figure 3.4 elaborates the boundary condition of the laser-irradiated surface.

Before solving the governing equation subjected to the given boundary conditions, variables need to be grouped into dimensionless groups/variables so that they can almost

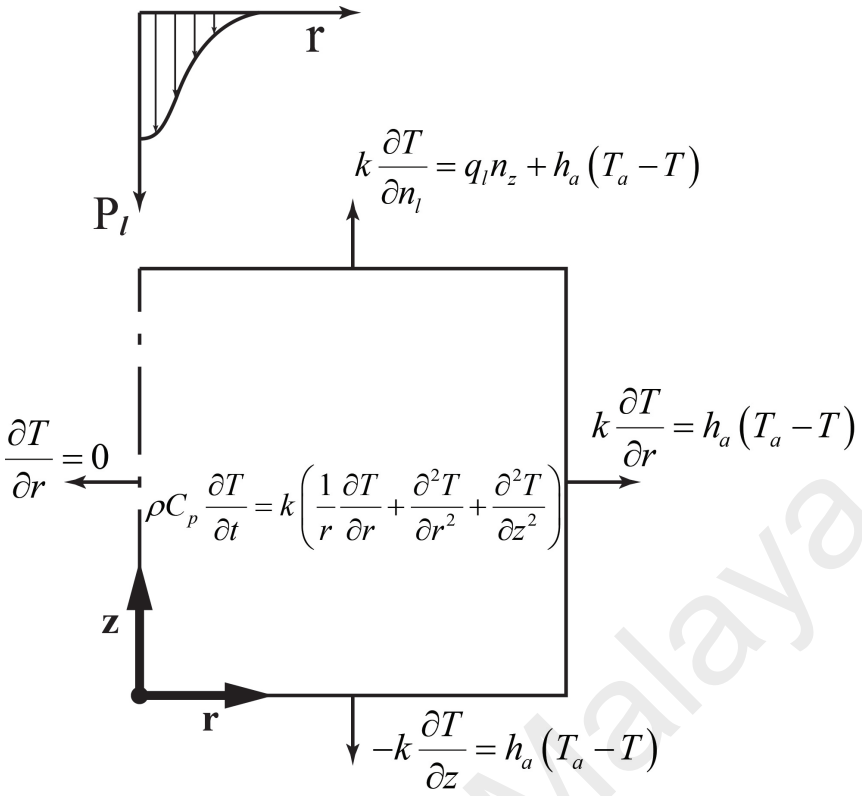

Figure 3.3: Governing equation and boundary conditions

have the same order, which helps in increasing the solution accuracy. Moreover, non-dimensionalization reduces the variables number and provides a clear idea about the impact of the variables on each other in the same group. Additionally, for each value of dimensionless group, different combinations of its variables values can exist which gives an economic expression of the experimental or numerical work (Steen & Mazumder, 2010). Consequently, the following dimensionless variables (as given in Kim, 2011) are introduced

$$\begin{aligned} r^* &= \frac{r}{r_b}, & B_i &= h_a \frac{r_b}{k}, & T^* &= \frac{T - T_a}{T_m - T_a}, \\ z^* &= \frac{z}{r_b}, & dt^* &= dt \frac{\lambda}{r_b^2}, & N_k &= \frac{k\,(T_m - T_a)}{r_b\,\alpha_l\,I_l} \end{aligned} \tag{3.3}$$

where $I_l = \frac{P_l}{\pi r_b^2}$ is the laser beam intensity. The governing and boundary conditions equations in dimensionless variables (after dropping asterisk for convenience) are:

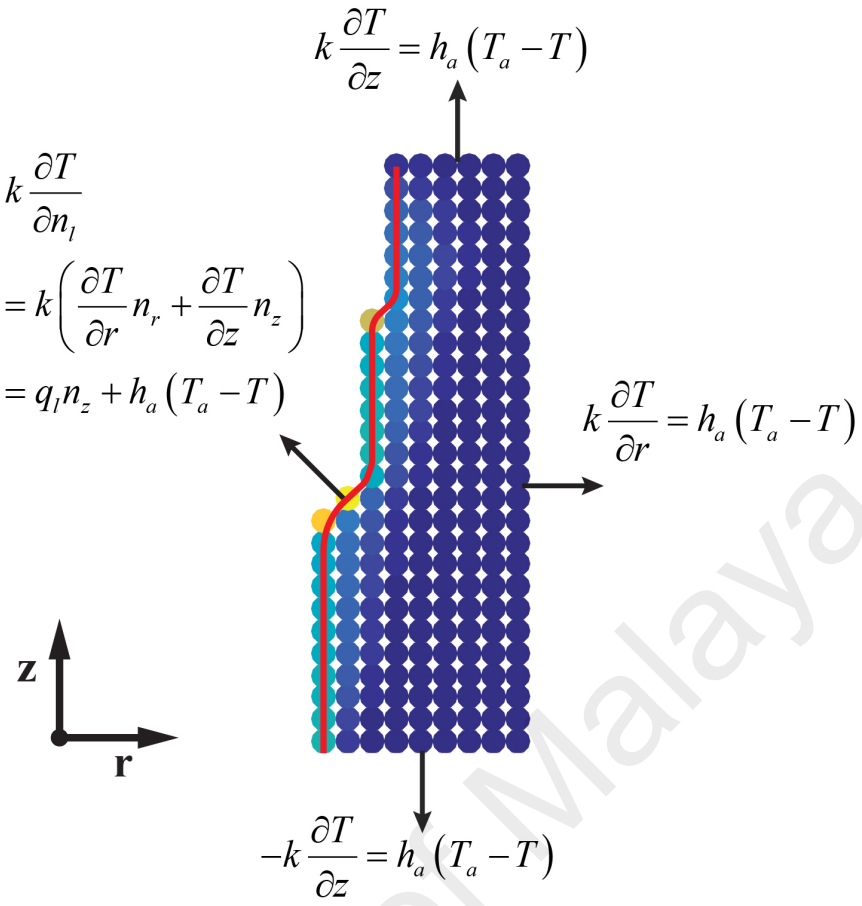

Figure 3.4: Boundary condition of laser-irradiated surface

$$
\begin{aligned}
&\frac{\partial T}{\partial t} = \left(\frac{1}{r}\frac{\partial T}{\partial r} + \frac{\partial T^2}{\partial r^2} + \frac{\partial T^2}{\partial z^2}\right) && \text{in } \Omega\,, \\
&\frac{\partial T}{\partial n_l} = \frac{e^{-2r^2}}{N_k}n_z - B_i T && \text{on } \Gamma_l, \\
&\frac{\partial T}{\partial r} = -B_i T && \text{on } r = l_r, \\
&\frac{\partial T}{\partial z} = B_i T && \text{on } z = 0, \\
&\frac{\partial T}{\partial r} = 0 && \text{on } r = 0.
\end{aligned}
\tag{3.4}
$$

The temperature and its spatial derivatives in Equation (3.4) will be approximated by MLPG, RPIM and SSPH, thus entailing the derivation of shape functions as follows in the subsequent sections. For each method, the whole domain Ω is assumed to be discretized into N particles with n neighboring particles of arbitrary particle $\mathbf{x}$ inside its support domain with radius h as shown in Figure 3.5.

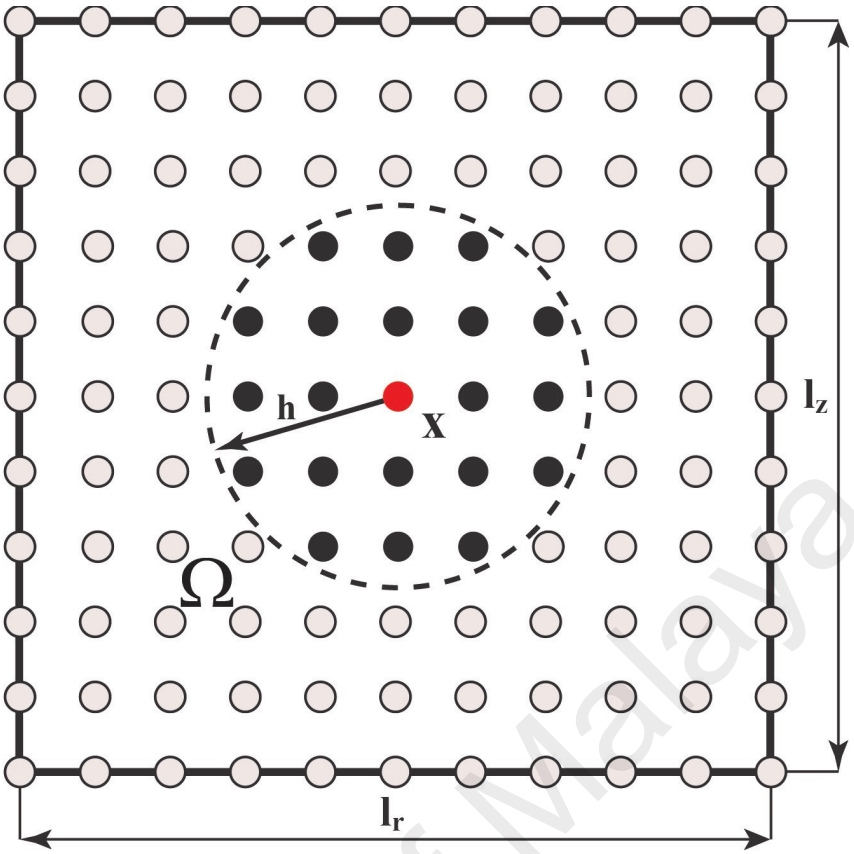

Figure 3.5: Support domain of arbitrary particle **x** and its neighboring particles

3.3 Mehsfree Collocation Methods

3.3.1 Meshless Local Petrov-Galerkin (MLPG)

For both global and weak-form methods methods, the moving least square (MLS) approximation technique is widely used for constructing shape functions for a set of neighboring particles inside the support domain defined for the particle of interest. MLS approximation was introduced as a mathematical tool for surface construction and data fitting (Lancaster & Salkauskas, 1981; Lancaster & estutis Šalkauskas, 1986). In heat transfer problems, MLS was used in approximating the temperature field for both strong and weak form meshfree methods (Singh, 2004; Wu, Shen, & Tao, 2007; Wu & Tao, 2008; Ahmadi et al., 2010). However, MLS approximation does not provide shape functions with Kronecker delta function property. As a result, special treatment is required in imposing essential boundary conditions for weak form methods such as Lagrange multiplier method (Lu, Belytschko, & Gu, 1994), transformation method (Atluri, Kim, & Cho, 1999), penalty approach (G.R. Liu & Reddy, 2002) or direct interpolation method (Liu & Gu, 2005). On the other hand, for weighted least square

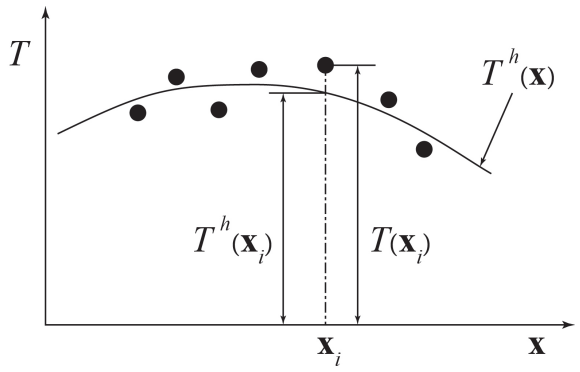

Figure 3.6: Approximated temperature $T^h(\mathbf{x_i})$ and the nodal temperature $T(\mathbf{x_i})$ in MLS approximation

(WLS) approximation, which can be viewed as a special case of MLS, the polynomials coefficients are constant and not function of the point of interest. Consequently, WLS shape functions are piecewise and the approximation is not moving continuously over the entire domain unlike in the case of MLS. Therefore, MLS has been always of primary interest in approximating the field variable for global weak-form methods.

MLS local approximation

For 2D axisymmetric problem with the whole domain discretized into N particles, at an arbitrary particle $\mathbf{x} = (r, z)$ with n neighboring particles in its local support domain, its temperature $T(\mathbf{x})$ can be approximated (as shown in Figure 3.6) by

$$T^h(\mathbf{x}) = \sum_{j=1}^{m} P_j(\mathbf{x})\, a_j = \mathbf{P^T}(\mathbf{x})\, \mathbf{a}(\mathbf{x}) \tag{3.5}$$

where $\mathbf{P}(\mathbf{x})$ is the polynomial basis function which has m monomials. To ensure completeness, monomials are obtained from Pascal's triangle. For example, $\mathbf{P}(\mathbf{x})$ can be linear, quadratic, or cubic basis when $m = 3$, $m = 6$, or $m = 10$, respectively, as follows

$$\begin{aligned} \mathbf{P}^T(\mathbf{x}) &= [1, r, z], && m = 3 \\ \mathbf{P}^T(\mathbf{x}) &= [1, r, z, r^2, rz, z^2], && m = 6 \\ \mathbf{P}^T(\mathbf{x}) &= [1, r, z, r^2, rz, z^2, r^3, r^2 z, rz^2, z^3], && m = 10. \end{aligned} \tag{3.6}$$

In Equation (3.5), coefficient vector $\mathbf{a}(\mathbf{x})$ is given by

$$\mathbf{a}(\mathbf{x})^T = \{\ a_1(\mathbf{x}) \quad a_2(\mathbf{x}) \quad \cdots \quad a_m(\mathbf{x})\ \}. \tag{3.7}$$

In order to determine $\mathbf{a}(\mathbf{x})$, the weighted discrete $\mathbf{L}_2$ norm, where $W_i(\mathbf{x})$ is the neighbor weight, is given as

$$J = \sum_{i=1}^{n} W_i(\mathbf{x}) \left[\mathbf{P}^T(\mathbf{x_i})\mathbf{a}(\mathbf{x}) - T_i\right]^2 \tag{3.8}$$

and minimized by differentiating with respect to $\mathbf{a}(\mathbf{x})$

$$\partial J / \partial \mathbf{a}(\mathbf{x}) = 0. \tag{3.9}$$

This results in the following set of equations

$$\mathbf{A}(\mathbf{x})\,\mathbf{a}(\mathbf{x}) = \mathbf{B}(\mathbf{x})\mathbf{T_s}, \tag{3.10}$$

where $\mathbf{T}_s$ is the vector of neighboring particles temperatures

$$\mathbf{T}_s = \begin{bmatrix} T_1 & T_2 & \cdots & T_n \end{bmatrix}^T, \tag{3.11}$$

and matrices $\mathbf{A}(\mathbf{x})$ and $\mathbf{B}(\mathbf{x})$ are defined by

$$\mathbf{A}(\mathbf{x})_{(m\times m)} = \sum_{i=1}^{n} W_i(\mathbf{x})\,\mathbf{P}(\mathbf{x_i})\ \mathbf{P^T}(\mathbf{x_i}) \tag{3.12}$$

and

$$\mathbf{B}(\mathbf{x})_{(m\times n)} = \begin{bmatrix} W_1(\mathbf{x})\,\mathbf{P}(\mathbf{x_1}) & W_2(\mathbf{x})\,\mathbf{P}(\mathbf{x_2}) & \cdots & W_n(\mathbf{x})\,\mathbf{P}(\mathbf{x_n}) \end{bmatrix}. \tag{3.13}$$

By solving Equation (3.10) for $\mathbf{a}(\mathbf{x})$

$$\mathbf{a}(\mathbf{x}) = \mathbf{A}^{-1}(\mathbf{x})\,\mathbf{B}(\mathbf{x})\,\mathbf{T_s} \tag{3.14}$$

and substituting into Equation (3.5), the approximated temperature can be obtained

$$T^h(\mathbf{x}) = \sum_{i=1}^{n} \phi_i(\mathbf{x}) T_i = \mathbf{\Phi}^T(\mathbf{x})\mathbf{T_s} \tag{3.15}$$

where

$$\begin{aligned}\boldsymbol{\Phi}^T(\mathbf{x}) &= \overbrace{\mathbf{P}^T(\mathbf{x})}^{(1\times m)}\ \overbrace{\mathbf{A}^{-1}(\mathbf{x})}^{(m\times m)}\ \overbrace{\mathbf{B}(\mathbf{x})}^{(m\times n)} \\ &= \left\{ \begin{array}{cccc} \phi_1(\mathbf{x}) & \phi_2(\mathbf{x}) & \cdots & \phi_n(\mathbf{x}) \end{array} \right\}_{(1\times n)}\end{aligned} \tag{3.16}$$

is the vector of local shape functions associated with the neighboring particles of particle $(\mathbf{x})$.

In other words, the shape function can be written as

$$\phi_i(\mathbf{x}) = \sum_{j=1}^{m} P_j(\mathbf{x}) \left(\mathbf{A^{-1}}(\mathbf{x})\, \mathbf{B}(\mathbf{x})\right)_{ji} = \mathbf{P}^T(\mathbf{x}) \left(\mathbf{A^{-1}}\, \mathbf{B}\right), \tag{3.17}$$

while its spatial derivative can be given by

$$\phi_{i,\gamma}(\mathbf{x}) = \sum_{j=1}^{m} p_{j,\gamma}(\mathbf{A^{-1}B})_{ji} + p_j \left(\mathbf{A^{-1}B}_{,\gamma} + \mathbf{A}^{\mathbf{-1}}_{,\boldsymbol{\gamma}}\mathbf{B}\right)_{ji}, \tag{3.18}$$

where γ denotes the spatial derivative, and $\mathbf{A}^{-1}_{,\gamma}$ is defined as

$$\mathbf{A}^{-1}_{,\gamma} = -\mathbf{A^{-1}}\, \mathbf{A}_{,\gamma}\, \mathbf{A^{-1}}. \tag{3.19}$$

WLS local approximation

As follows, WLS approximation is briefly introduced while keeping the same matrices notations as in MLS. For an arbitrary particle $\mathbf{x}$ in axisymmetric two-dimensional domain, its temperature field $T(\mathbf{x})$ can be approximated by polynomial basis:

$$T(\mathbf{x}) \approx T^h(\mathbf{x}) = \sum_{j=1}^{m} P_j(\mathbf{x})\, a_j = a_1 + a_2 r + a_3 z + \cdots + P_m(\mathbf{x})\, a_m$$

$$= \left\{ \begin{array}{ccccc} 1 & r & z & \cdots & P_m(\mathbf{x}) \end{array} \right\} \left\{ \begin{array}{c} a_1 \\ a_2 \\ \\ \vdots \\ \\ a_m \end{array} \right\} = \mathbf{P^T a} \tag{3.20}$$

where a_j $(j = 1 \ \ldots \ m)$ are the coefficients to be calculated, while $\mathbf{P}$ is the monomial basis vector as given in Equation (3.6).

To find the value of $\mathbf{a}$ in Equation (3.20), n neighboring particles are searched for within the local support domain radius of point $(\mathbf{x})$. Satisfying Equation (3.20) at all the neighboring particles leads to the following set of equations:

$$\mathbf{T}_s = \mathbf{P}_{m_{(n\times m)}}\, \mathbf{a}_{(m\times 1)} \tag{3.21}$$

where the polynomial moment matrix, $\mathbf{P}_m$, is defined by

$$\mathbf{P}_m = \begin{bmatrix} 1 & r_1 & z_1 & \cdots & P(\mathbf{x}_1) \\ 1 & r_2 & z_2 & \cdots & P(\mathbf{x}_2) \\ \vdots & \vdots & \vdots & \ddots & \vdots \\ 1 & r_n & z_n & \cdots & P(\mathbf{x}_n) \end{bmatrix}_{(n\times m)} , \tag{3.22}$$

Equation (3.21) is solved for $\mathbf{a}$ using the WLS by minimizing the weighted discrete $\mathbf{L}_2$ norm

$$J = \sum_{i=1}^{n} W_i \left[T^h(\mathbf{x_i}) - T(\mathbf{x_i}) \right]^2 \tag{3.23}$$

where $W_i\,(i = 1, 2, \ldots, n)$ is the weight associated with each neighboring particle. The minimization

$$\partial J/\partial \mathbf{a} = 0 \tag{3.24}$$

leads to the following equation

$$\mathbf{P}_{\mathbf{m}}^{T}\,\mathbf{W}\,\mathbf{P}_{\mathbf{m}}\,\mathbf{a} = \mathbf{P}_{\mathbf{m}}^{T}\,\mathbf{W}\,\mathbf{T}_{s} \tag{3.25}$$

where $\mathbf{W}_{(n\times n)}$ is the diagonal matrix of neighboring particles weights.

By following $\mathbf{A}$ and $\mathbf{B}$ definitions in Equations (3.12) and (3.13), Equation (3.25) can be written as

$$\mathbf{a} = \left(\mathbf{P}_{m}^{T}\,\mathbf{W}\mathbf{P}_{m}\right)^{-1}\,\left(\mathbf{P}_{m}^{T}\,\mathbf{W}\right)\,\mathbf{T}_{s} = \mathbf{A}^{-1}\,\mathbf{B}\,\mathbf{T}_{s}. \tag{3.26}$$

By substituting Equation (3.26) into Equation (3.20), the approximate temperature $T^{h}(\mathbf{x})$ can be calculated by

$$T^{h}(\mathbf{x}) = \mathbf{P}^{T}(\mathbf{x})\,\mathbf{a} = \mathbf{P}^{T}(\mathbf{x})\,\mathbf{A}^{-1}\,\mathbf{B}\,\mathbf{T}_{s} = \mathbf{\Phi}^{T}\,\mathbf{T}_{s}, \tag{3.27}$$

where $\mathbf{\Phi}$ is the vector of local shape functions and defined by

$$\mathbf{\Phi}^{T} = \mathbf{P}^{T}(\mathbf{x})\,\mathbf{A}^{-1}\,\mathbf{B} = \left\{ \begin{array}{cccc} \phi_1 & \phi_2 & \cdots & \phi_n \end{array} \right\}_{(1\times n)}, \tag{3.28}$$

while its spatial derivative is given as

$$\mathbf{\Phi}_{,\gamma}^{T} = \mathbf{P}_{,\gamma}^{T}(\mathbf{x})\,\mathbf{A}^{-1}\,\mathbf{B} = \left\{ \begin{array}{cccc} \phi_1 & \phi_2 & \cdots & \phi_n \end{array} \right\}_{(1\times n)}, \tag{3.29}$$

It can be clearly seen that the main difference between MLS and WLS is the coefficients vector $\mathbf{a}$ is function of the point $\mathbf{x}$ in MLS (in Equation (3.14)) unlike in the case of WLS (in Equation (3.26)). This comes from the dependence of the neighboring particle weight function $W_i(\mathbf{x})$ on the location of point $(\mathbf{x})$. This leads to continuous temperature

approximation over the whole domain when MLS is used in case of global weak-form methods (e.g. EFG). Moreover, it means that the approximated temperature field is ensured to be continuous over the entire domain when the neighboring nodes enter/leave the local support domain. However, the present work uses a direct collocation strong-form not a global weak-form method, which makes this global compatibility not an issue (Liu & Gu, 2005). Additionally, for both MLS and WLS, the number of neighboring particles in the support domain n should be sufficiently higher than the number of monomials m in order to ensure the well condition of matrix $\mathbf{A}$ (in Equations (3.14) and (3.26)) and the existence of its inversion.

Weight functions

It can be noticed that the matrices $\mathbf{A}$ and $\mathbf{B}$ depends on the weight/kernel function. Therefore, their smoothness depends on that of the used weight function. For the present simulation, three different popular weight functions are tested for both MLS and WLS approximations in the present model. The three weight functions are

Cubic spline (Monaghan, 2005)

$$W(d)=\frac{1}{6}\begin{cases}(2-2\,d)^3-4\,(1-2\,d)^3\,, & 0\le d<0.5\\ (2-2\,d)^3\,, & 0.5\le d\le 1\\ 0, & 1<d\end{cases}, \tag{3.30}$$

Quartic spline (Wu & Tao, 2008)

$$W(d)=\begin{cases}1-6\,d^2+8\,d^3-3\,d^4, & 0\le d\le 1\\ 0, & 1<d\end{cases}, \tag{3.31}$$

Gaussian (Tsai et al., 2012)

$$W(d) = \frac{1}{1-e^{-4}} \begin{cases} e^{-4\,d} - e^{-4}, & 0 \le d \le 1 \\ 0, & 1 < d \end{cases}, \tag{3.32}$$

where $d = \frac{\|\mathbf{x}-\mathbf{x_i}\|}{h}$ is the normalized Euclidean distance between the particle of interest and its neighbor.

3.3.2 Radial Point Interpolation Method (RPIM)

Due to their dimensionality-independence, easy implementation and integration-free properties, radial basis function (RBF) collocation methods have proved to be a reliable tool in solving partial differential equations (PDEs), multi-variate scattered data processing, machine learning and neural networks (Wang & Liu, 2002a; Chen, Fu, & Chen, 2014). Their applications in solving PDEs have been widely reported in fields of solid mechanics and fluid dynamics (Kansa, 1990a, 1990b; Liu, Zhang, Gu, & Wang, 2005a; Gerace, Divo, & Kassab, 2006; Divo & Kassab, 2007; Dai et al., 2011; Divo & Kassab, 2014; Mavrič & Šarler, 2015). On the other hand, due to the solution accuracy and convergence sensitivity to the shape parameters in RBFs, attention and effort have been given to evaluate the optimal shape parameters (Wang & Liu, 2002b; Huang, Lee, & Cheng, 2007; Fornberg & Piret, 2008; Cheng, 2012; Iurlaro, Gherlone, & Sciuva, 2014).

At an arbitrary point $\mathbf{x}$ with n neighboring particles in its support domain for 2D problem, temperature $T(\mathbf{x})$ can be approximated by both n RBFs and m polynomials

$$T(\mathbf{x}) = \sum_{i=1}^{n} R_i(\mathbf{x})\, a_i + \sum_{j=1}^{m} P_j(\mathbf{x})\, b_j = \mathbf{R}(\mathbf{x})^{\mathbf{T}}\, \mathbf{a} + \mathbf{p}(\mathbf{x})\, \mathbf{b} \tag{3.33}$$

where a_i & b_j are coefficients to be calculated, $P_j(\mathbf{x})$ is linear polynomial basis and $R_i(\mathbf{x})$ is the RBF where the two commonly used RBFs, Multi-quadrics RBF (MQ-RBF) and Exponential/Gaussian RBF (EXP-RBF), are defined by

$$R_i(\boldsymbol{\xi}) = \left[\xi_i + (\alpha_m d_c)^2\right]^q \qquad \text{and}$$
$$R_i(\boldsymbol{\xi}) = \exp\left[-\alpha_e \left(\frac{\xi_i}{d_c}\right)^2\right] \tag{3.34}$$

respectively, where $\xi_i = \sqrt{(r-r_i)^2 + (z-z_i)^2}$ is the Euclidean distance, d_c is the characteristic length which is equal to the average particles spacing within the support domain, and α_m, q and α_e are shape parameters (Liu & Gu, 2005).

In order to evaluate the coefficients a_i & b_j, Equation (3.33) is applied at each particle in the support domain which leads to the matrix form

$$\mathbf{T_s} = \mathbf{R_0}\,\mathbf{a} + \mathbf{P_m}\,\mathbf{b} \tag{3.35}$$

where the vector of all the particles temperatures in the local support domain is

$$\mathbf{T_s} = \begin{bmatrix} T_1 & T_2 & \cdots & T_n \end{bmatrix}^T, \tag{3.36}$$

the moment matrix of RBFs is

$$\mathbf{R_0} = \begin{bmatrix} R_1(\xi_1) & R_2(\xi_1) & \cdots & R_n(\xi_1) \\ R_1(\xi_2) & R_2(\xi_2) & \cdots & R_n(\xi_2) \\ \vdots & \vdots & \ddots & \vdots \\ R_1(\xi_n) & R_2(\xi_n) & \cdots & R_n(\xi_n) \end{bmatrix}_{(n\times n)}, \tag{3.37}$$

the polynomial moment matrix is

$$\mathbf{P_m} = \begin{bmatrix} 1 & r_1 & z_1 & \cdots & P(\mathbf{x}_1) \\ 1 & r_2 & z_2 & \cdots & P(\mathbf{x}_2) \\ \vdots & \vdots & \vdots & \vdots & \vdots \\ 1 & r_n & z_n & \cdots & P(\mathbf{x}_n) \end{bmatrix}_{(n \times m)}, \tag{3.38}$$

the vector of RBFs coefficients is

$$\mathbf{a} = \left\{ \begin{array}{cccc} a_1 & a_2 & \cdots & a_n \end{array} \right\}^T, \tag{3.39}$$

the vector of polynomials coefficients is

$$\mathbf{b} = \left\{ \begin{array}{cccc} b_1 & b_2 & \cdots & b_m \end{array} \right\}^T. \tag{3.40}$$

The augmented polynomials need to satisfy the following requirement

$$\sum_{i=1}^{n} P_j(\mathbf{x}_i)\, a_i = \mathbf{P}_\mathbf{m}^T \mathbf{a} = \mathbf{0}, \quad j = 1, 2, \ldots, m \tag{3.41}$$

where m is the number of monomials. Combining both Equation (3.35) and Equation (3.41), the following equations set is obtained

$$\widetilde{\mathbf{T}}_\mathbf{s} = \begin{bmatrix} \mathbf{T_s} \\ \mathbf{0} \end{bmatrix} = \underbrace{\begin{bmatrix} \mathbf{R_0} & \mathbf{P_m} \\ \mathbf{P}_\mathbf{m}^T & \mathbf{0} \end{bmatrix}}_{\mathbf{G}} \underbrace{\begin{bmatrix} \mathbf{a} \\ \mathbf{b} \end{bmatrix}}_{\mathbf{a_0}} = \mathbf{G}\,\mathbf{a_0} \tag{3.42}$$

where

$$\mathbf{a_0} = \left\{ \begin{array}{cccccccc} a_1 & a_2 & \cdots & a_n & b_1 & b_2 & \cdots & b_m \end{array} \right\}^T = \mathbf{G^{-1}}\widetilde{\mathbf{T}}_\mathbf{s} \tag{3.43}$$

and

$$\widetilde{\mathbf{T}}_\mathbf{s} = \left\{ \begin{array}{ccccc} T_1 & T_2 & \cdots & T_n & \mathbf{0}_{(1\times m)} \end{array} \right\}^T \tag{3.44}$$

Equation (3.33) can be written as:

$$T(\mathbf{x}) = [\mathbf{R}(\mathbf{x}) \quad \mathbf{P}(\mathbf{x})]\,\mathbf{G}^{-1}\widetilde{\mathbf{T}}_{\mathbf{s}} = \widetilde{\mathbf{\Phi}}(\mathbf{x})\,\widetilde{\mathbf{T}}_{\mathbf{s}} \tag{3.45}$$

where

$$\widetilde{\mathbf{\Phi}}(\mathbf{x}) = \left\{ \begin{array}{ccccccc} \phi_1 & \phi_2 & \cdots & \phi_n & \phi_{n+1} & \cdots & \phi_{n+m} \end{array} \right\}. \tag{3.46}$$

According to the particles temperatures, the shape functions vector $\mathbf{\Phi}(\mathbf{x})$ is obtained as

$$\mathbf{\Phi}(\mathbf{x}) = \left\{ \begin{array}{cccc} \phi_1 & \phi_2 & \cdots & \phi_n \end{array} \right\} \tag{3.47}$$

and Equation (3.45) can be written as

$$T(\mathbf{x}) = \mathbf{\Phi}(\mathbf{x})\,\mathbf{T}_{\mathbf{s}} = \sum_{i=1}^{n} \phi_i T_i. \tag{3.48}$$

Additionally, the temperature spatial derivatives can be calculated by

$$T_{,\gamma}(\mathbf{x}) = \mathbf{\Phi}_{,\boldsymbol{\gamma}}(\mathbf{x})\,\mathbf{T}_{\mathbf{s}} = \sum_{i=1}^{n} \phi_{i,\gamma} T_i \tag{3.49}$$

where γ denotes the spatial derivative of the shape function.

Since the introduction of polynomials is for completeness (Wertz, Kansa, & Ling, 2006), only the pure radial basis functions will be used in the present work for local approximation. For MQ-RBFs introduced in Equation (3.34), the shape parameters were investigated in Wang and Liu, 2002b; Liu and Gu, 2005 showing their influence on the condition number of matrix $\mathbf{G}$ or $\mathbf{R}$ (for pure radial RBF) in Equation (3.42), and hence the accuracy of the interpolation. It was reported that the shape parameter q heavily affects the matrix condition number, and its value of 1.03 is the optimal for the reported solid mechanics problems and will be used here. On the other hand, a careful attention should be paid in selecting the shape parameter α_m value, since higher values increase the interpolation accuracy while degrades the solution stability due to the badly conditioned moment matrix $\mathbf{R}$ and vice versa.

3.3.3 Symmetric Smoothed Particle Hydrodynamics (SSPH)

In Zhang and Batra, 2008, SSPH method was introduced as a new meshless approach for approximating the field variables and their derivatives using only the coordinates of the domain particles. In this method, two main advantages can be obtained over the other meshfree methods such as MLS and modified smoothed particle hydrodynamics (MSPH). First, local nodal field variable and its spatial derivative can be derived with inverting a symmetric matrix. Therefore, huge amount of computational load and time can be significantly saved. Second, this method does not depend on the spatial derivatives of the kernel function for approximating the nodal field variable and its spatial derivative. Thus, a broader class of kernel functions can be addressed without limitation. In other words, different shape functions can be derived for approximating the domain function and its derivatives. In this way, the spatial derivatives of the trial solution from different shape functions yield more accurate solution than that derived from differentiating the shape functions.

The SSPH solution of elastic problems was discussed in Zhang and Batra, 2008 and compared to those of MLS and RKPM with different six kernel functions. SSPH yielded promising accurate solution compared to MLS and RKPM against the exact solution. While in Batra and Zhang, 2007, both weak and strong forms of SSPH were proposed for addressing the elastic problems while monitoring the required CPU time for both forms. In summary, strong form consumes less computational resources with less accurate results, while reverse holds for the weak form. Additionally, SSPH was introduced in the solution of two-dimensional heat transfer problems while noting the less accurate results for non-homogeneous problems (Mugan, 2012).

For two arbitrary points $\mathbf{x} = \{\boldsymbol{\xi}, \mathbf{x}^{(i)}\}$ in the domain, the Taylor series expansion of temperature at point $\mathbf{x}^{(i)}$ can be expressed by

$$T(\boldsymbol{\xi}) = T\left(\mathbf{x}^{(i)}\right) + \frac{\partial T}{\partial x_\alpha^{(i)}}\left(\xi_\alpha - x_\alpha^{(i)}\right) + \frac{1}{2}\frac{\partial^2 T}{\partial x_\alpha^{(i)} \partial x_\beta^{(i)}}\left(\xi_\alpha - x_\alpha^{(i)}\right)\left(\xi_\beta - x_\beta^{(i)}\right) + \cdots \quad (3.50)$$

where repeated indices α and β are summed over their ranges (i.e. r, z), and third and higher order terms are neglected.

In matrix notation, Equation (3.50) can be rewritten as

$$T(\boldsymbol{\xi}) = \mathbf{P}\left(\boldsymbol{\xi}, \mathbf{x}\right) \mathbf{Q}\left(\mathbf{x}\right) \tag{3.51}$$

where

$$\mathbf{Q}\left(\mathbf{x}\right) = \left[T^{(i)}, T_{x_1}^{(i)}, T_{x_2}^{(i)}, \frac{1}{2}T_{x_1x_1}^{(i)}, \frac{1}{2}T_{x_2x_2}^{(i)}, T_{x_1x_2}^{(i)}, \right]^T, \tag{3.52}$$

$$\mathbf{P}\left(\boldsymbol{\xi}, \mathbf{x}\right) = \left\{ \begin{array}{c} 1, \xi_1 - x_1^{(i)}, \xi_2 - x_2^{(i)}, \xi_3 - x_3^{(i)}, \\ \left(\xi_1 - x_1^{(i)}\right)^2, \left(\xi_2 - x_2^{(i)}\right)^2, \left(\xi_3 - x_3^{(i)}\right)^2, \\ \left(\xi_1 - x_1^{(i)}\right)\left(\xi_2 - x_2^{(i)}\right), \\ \left(\xi_2 - x_2^{(i)}\right)\left(\xi_3 - x_3^{(i)}\right), \\ \left(\xi_3 - x_3^{(i)}\right)\left(\xi_1 - x_1^{(i)}\right) \end{array} \right\}, \tag{3.53}$$

$$T_i = T\left(\mathbf{x}^{(i)}\right), T_{x_\alpha i} = \frac{\partial T}{\partial x_\alpha}\left(\mathbf{x}^{(i)}\right), T_{x_\alpha x_\beta i} = \frac{\partial^2 T}{\partial x_\alpha \partial x_\beta}\left(\mathbf{x}^{(i)}\right) \tag{3.54}$$

$\mathbf{Q}\left(\mathbf{x}\right)$ is the matrix of unknown temperature and its spatial derivatives at point (i). In search of a symmetric matrix to be solved, both sides of Equation (3.51) are right multiplied with kernel function $W(\boldsymbol{\xi}, \mathbf{x})$ and $\mathbf{P}(\boldsymbol{\xi}, \mathbf{x})^T$

$$\begin{aligned} T(\boldsymbol{\xi})\, W(\boldsymbol{\xi}, \mathbf{x})\, \mathbf{P}(\boldsymbol{\xi}, \mathbf{x})^T &= \mathbf{P}\left(\boldsymbol{\xi}, \mathbf{x}\right) \mathbf{Q}\left(\mathbf{x}\right) W(\boldsymbol{\xi}, \mathbf{x})\, \mathbf{P}(\boldsymbol{\xi}, \mathbf{x})^T \\ &= \left[\mathbf{P}(\boldsymbol{\xi}, \mathbf{x})^T W(\boldsymbol{\xi}, \mathbf{x})\, \mathbf{P}\left(\boldsymbol{\xi}, \mathbf{x}\right)\right] \mathbf{Q}\left(\mathbf{x}\right) \end{aligned} \tag{3.55}$$

Equation (3.55) is evaluated at each neighboring particle inside the kernel compact support, and both sides are summed over all the neighboring particles. For $N(\mathbf{x})$ neighboring particles, Equation (3.55) can be written as

$$\begin{aligned}&\sum_{j=1}^{N(\mathbf{x})} T\left(\boldsymbol{\xi}^{g(j)}\right) W\left(\boldsymbol{\xi}^{g(j)}, \mathbf{x}\right) \mathbf{P}\left(\boldsymbol{\xi}^{g(j)}, \mathbf{x}\right)^T \\ &= \sum_{j=1}^{N(\mathbf{x})} \left[\mathbf{P}\left(\boldsymbol{\xi}^{g(j)}, \mathbf{x}\right)^T W\left(\boldsymbol{\xi}^{g(j)}, \mathbf{x}\right) \mathbf{P}\left(\boldsymbol{\xi}^{g(j)}, \mathbf{x}\right)\right] \mathbf{Q}(\mathbf{x})\end{aligned} \tag{3.56}$$

where $g(j)$ is the global index of the neighboring particle, and $\boldsymbol{\xi}^{g(j)}$ is its coordinate.

With the following definitions

$$\mathbf{H}(\boldsymbol{\xi}, \mathbf{x}) = \left[\mathbf{P}^T\left(\boldsymbol{\xi}^{g(1)}, \mathbf{x}\right),\ \mathbf{P}^T\left(\boldsymbol{\xi}^{g(2)}, \mathbf{x}\right), \cdots,\ \mathbf{P}^T\left(\boldsymbol{\xi}^{g(N(\mathbf{x}))}, \mathbf{x}\right)\right],$$

$$\mathbf{W}(\boldsymbol{\xi}, \mathbf{x}) = \begin{bmatrix} W\left(\boldsymbol{\xi}^{g(1)}, \mathbf{x}\right) & 0 & \cdots & 0 \\ 0 & W\left(\boldsymbol{\xi}^{g(2)}, \mathbf{x}\right) & \cdots & 0 \\ \vdots & \vdots & \ddots & \vdots \\ 0 & 0 & 0 & W\left(\boldsymbol{\xi}^{g(N(\mathbf{x}))}, \mathbf{x}\right) \end{bmatrix}, \tag{3.57}$$

$$\mathbf{F}^{(\mathbf{x})}(\boldsymbol{\xi}, \mathbf{x}) = \left[T\left(\boldsymbol{\xi}^{g(1)}\right), T\left(\boldsymbol{\xi}^{g(2)}\right), \ldots, T\left(\boldsymbol{\xi}^{g(N(\mathbf{x}))}\right)\right]^T$$

Equation (3.56) can be rewritten as

$$\mathbf{H}(\boldsymbol{\xi}, \mathbf{x})\ \mathbf{W}(\boldsymbol{\xi}, \mathbf{x})\ \mathbf{F}^{(\mathbf{x})}(\boldsymbol{\xi}, \mathbf{x}) = \mathbf{H}(\boldsymbol{\xi}, \mathbf{x})\ \mathbf{W}(\boldsymbol{\xi}, \mathbf{x})\ \mathbf{H}^T(\boldsymbol{\xi}, \mathbf{x})\ \mathbf{Q}(\boldsymbol{\xi}, \mathbf{x}). \tag{3.58}$$

With the definition of symmetric matrix $\mathbf{C}(\boldsymbol{\xi}, \mathbf{x}) = \mathbf{H}(\boldsymbol{\xi}, \mathbf{x})\ \mathbf{W}(\boldsymbol{\xi}, \mathbf{x})\ \mathbf{H}^T(\boldsymbol{\xi}, \mathbf{x})$ and

$\mathbf{D}(\boldsymbol{\xi}, \mathbf{x}) = \mathbf{H}(\boldsymbol{\xi}, \mathbf{x})\ \mathbf{W}(\boldsymbol{\xi}, \mathbf{x})$, Equation (3.58) will be

$$\mathbf{C}(\boldsymbol{\xi}, \mathbf{x})\ \mathbf{Q}(\boldsymbol{\xi}, \mathbf{x}) = \mathbf{D}(\boldsymbol{\xi}, \mathbf{x})\ \mathbf{F}^{(\mathbf{x})}(\boldsymbol{\xi}, \mathbf{x}) \tag{3.59}$$

and $\mathbf{Q}(\mathbf{x})$ can be expressed as

$$\begin{aligned} \mathbf{Q}(\mathbf{x}) &= \mathbf{C}(\boldsymbol{\xi}, \mathbf{x})^{-1}\ \mathbf{D}(\boldsymbol{\xi}, \mathbf{x})\ \mathbf{F}^{(\mathbf{x})}(\boldsymbol{\xi}, \mathbf{x}) \\ &= \mathbf{K}^{(\mathbf{x})}(\boldsymbol{\xi}, \mathbf{x})\ \mathbf{F}^{(\mathbf{x})}(\boldsymbol{\xi}, \mathbf{x}) \end{aligned} \tag{3.60}$$

where

$$\mathbf{K}^{(\mathbf{x})} = \mathbf{C}(\boldsymbol{\xi}, \mathbf{x})^{-1}\ \mathbf{D}(\boldsymbol{\xi}, \mathbf{x}) \tag{3.61}$$

is the local shape function matrix and $\mathbf{F}^{(\mathbf{x})}(\boldsymbol{\xi}, \mathbf{x})$ is the vector of temperature values at neighboring particles. Equation (3.60) can be written as following

$$Q_i(\mathbf{x}) = \sum_{j=1}^{N(\mathbf{x})} K_{ij}^{(\mathbf{x})}\ F_j^{(\mathbf{x})},\ \ i = 1, 2, \cdots, 6 \tag{3.62}$$

$\mathbf{Q}(\mathbf{x})$ has the approximated temperature value and its spatial derivatives;
$\mathbf{Q}(\mathbf{x}) = \left[T^h,\ T^h_{,r},\ T^h_{,z}, \frac{1}{2}T^h_{,rr}, \frac{1}{2}T^h_{,zz},\ T^h_{,rz}\right]^T$, where comma denotes spatial derivative, and superscript h denotes approximated value.

Weight functions

For the local approximation in this work, the following three different kernel functions from Zhang and Batra, 2008 will be used, and their numerical results will be compared with each other:

Cubic B-Spline

$$W(d) = \frac{G}{l_s^{\beta}} \begin{cases} 1 - 1.5\,d^2 + 0.75\,d^3, & 0 \le d < 1 \\ (2-d)^3/4, & 1 \le d < 2 \\ 0, & d \ge 2 \end{cases} \tag{3.63}$$

Quartic Spline

$$W(d) = \frac{G}{l_s^{\beta}} \begin{cases} 1 - 1.5\,d^2 + d^3 - \frac{3}{16}d^4, & 0 \le d < 2 \\ 0, & d \ge 2 \end{cases} \tag{3.64}$$

Revised Super Gauss

$$W(d) = \frac{G}{\left(l_s\sqrt{\pi}\right)^{\beta}} \begin{cases} \left(4 - d^2\right) e^{-a\,d^2}, & 0 \le d < 2 \\ 0, & d \ge 2 \end{cases} \tag{3.65}$$

where $d = \frac{r_{ij}}{h}$, r_{ij} is the Euclidean distance between the particle of interest *i* and its neighbor *j*, and $l_s = \frac{1}{2}h$ is the smoothing length. Following the discussion in Zhang and Batra, 2008, the value of G is not important in SSPH method, since it cancels out on both sides of Equation (3.56) and will be taken as unity here, β is the problem dimensionality which is two in this axisymmetric case, l_s will take both values of $\{1.2\Delta, 1.5\Delta\}$ to be tested and a in Super Revised Gauss function can be taken as 1.6.

3.4 Discretization of System Equations

After getting the shape functions, the governing equation and boundary conditions in Equation (3.4) can be discretized as follows:

$$\begin{aligned}
&\sum_{i=1}^{n} \phi_i \frac{\partial T_i}{\partial t} = \sum_{i=1}^{n} \left(\frac{1}{r}\phi_{i,r} + {\phi_{i,r}}^2 + {\phi_{i,z}}^2 \right) T_i && \text{in } \Omega \\
&\sum_{i=1}^{n} \phi_{i,n_l} T_i = \frac{e^{-2r^2}}{N_k} n_z - B_i \sum_{i=1}^{n} \phi_i\, T_i && \text{on } \Gamma_l, \\
&\sum_{i=1}^{n} \phi_{i,r} T_i = -B_i \sum_{i=1}^{n} \phi_i\, T_i && \text{on } r = l_r, \\
&\sum_{i=1}^{n} \phi_{i,z} T_i = B_i \sum_{i=1}^{n} \phi_i\, T_i && \text{on } z = 0, \\
&\sum_{i=1}^{n} \phi_{i,r} T_i = 0 && \text{on } r = 0.
\end{aligned} \tag{3.66}$$

In matrix form for the entire domain, the foregoing set of equations is written as:

$$\mathbf{M}\,\dot{\mathbf{T}} + \mathbf{K}\,\mathbf{T} = \mathbf{F} \tag{3.67}$$

where $\mathbf{T}$ is the temperature vector of the whole domain particles, $\mathbf{M}$ is the mass matrix, $\mathbf{K}$ is the stiffness matrix and $\mathbf{F}$ is the force vector. Crank-Nicolson method is used to temporally solve this transient equation in an iterative scheme. As a result, the solution is unconditionally stable irrespective of the time step size with second order accuracy in time. Therefore, the temperature temporal iterative scheme can be written as:

$$\mathbf{T}^{t+\Delta t} = \left[\mathbf{2}\,\mathbf{M} + \Delta t\,\mathbf{K}\right]^{-\mathbf{1}} \left[\left(\mathbf{2}\,\mathbf{M} - \Delta t\,\mathbf{K}\right)\mathbf{T}^{t} + \Delta t\left(\mathbf{F}^{t} + \mathbf{F}^{t+\Delta t}\right)\right] \tag{3.68}$$

3.5 Model Logic and Laser Absorptivity

3.5.1 Model Scheme Pseudocode and Flowchart

The model scheme is translated into the pseudocode, and its flowchart is depicted in Figure 3.7.

MATLAB model algorithm

```
Define domain particles in terms of metal properties and location
% Loop over time steps %
foreach time step do
    Calculate normal vector n̂ direction cosines at each laser-irradiated boundary
      particle
    % Loop over existing domain particles %
    foreach domain particle do
        Search for and loop over neighboring particles
        % Loop over neighboring particles %
        foreach neighboring particle do
            calculate shape functions
        Assemble global mass matrix M, stiffness matrix K and force vector F
    Calculate global temperature vector T^{t+t} in Equation (3.68)
    Remove molten particles and resize M, K and F
```

3.5.2 Laser Absorptivity

The material laser absorptivity is vital in a proper mathematical modeling of laser micromachining. Its value increases with higher temperature of the target material,

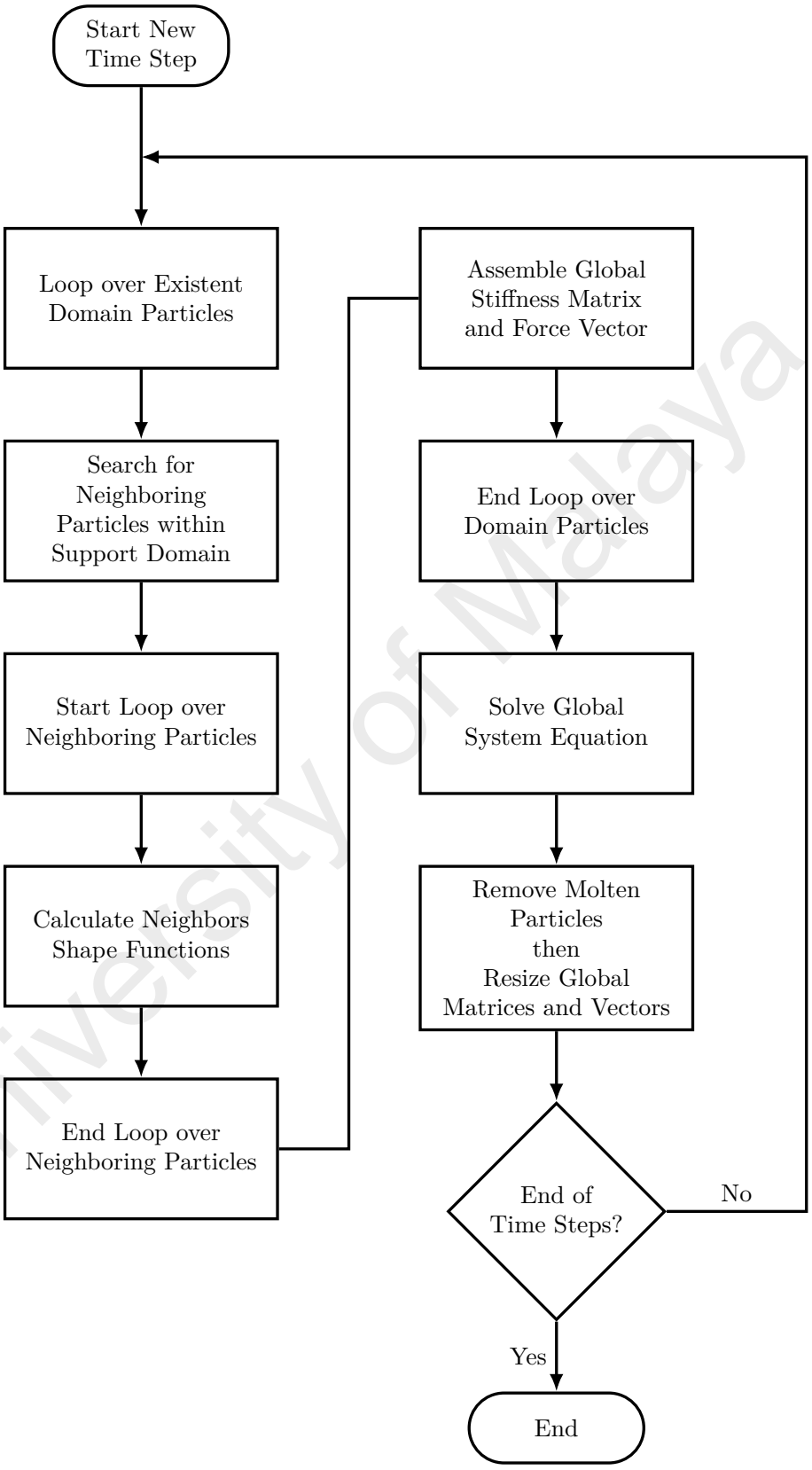

Figure 3.7: Flowchart of the model logic

shorter laser beam wavelength, deeper processed hole and thicker oxidation layer. For most metals at room temperature, the laser absorptivity is low, while it increases substantially with temperature with abrupt increase at the melting temperature (Xie, Kar, Rothenflue, & Latham, 1997; Bergström, 2008).

In Zhang and Faghri, 1999, the estimation of laser absorptivity proper value for numerical simulation of laser processing was thoroughly discussed. The absorptivity was assumed to take a value of unity in Ganesh et al., 1997a, 1997b (as cited in Zhang and Faghri, 1999) due to deep processed holes, high temperature and formation of plasma. However, a value of 0.85 was recommended in Kar et al., 1992 in a 2D axisymmtric simulation of laser drilling. This value was also called an effective absorptivity and considered in the simulation in Zhang and Faghri, 1999, and it will be used in the present work.

3.5.3 Model Standalone Application

Since the model is based on the employment of meshfree collocation methods, it is believed to have low computational load compared with mesh-based numerical methods. Therefore, it is viable and beneficial to convert the present model into a lightweight standalone application to be easily integrated into a GUI of a typical industrial laser machine. Such an integration can help identify the process parameters limitations and output instead of the costly experimentation. The GUI of this standalone application is shown in Figure 3.8, and more details on its code can be found in Appendix A.

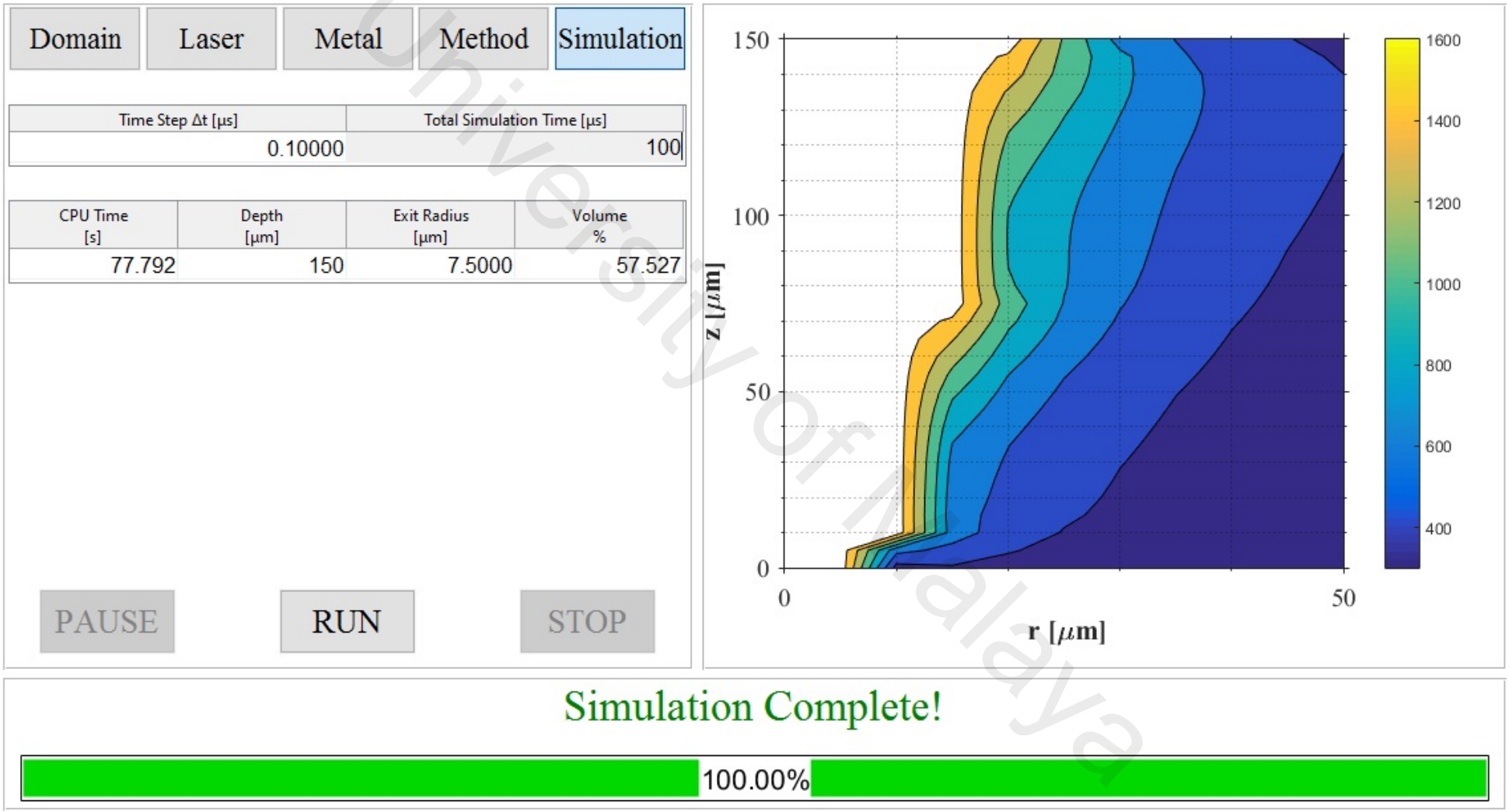

Figure 3.8: Graphical user interface of the proposed standalone application

CHAPTER 4: RESULTS AND DISCUSSION

4.1 Introduction

After constructing the numerical model as previously shown, this chapter shows the validation of the present model against a relevant mehsfree published work in addition to a set of experimental data collected from laser drilling of stainless steel and aluminum sheets.

4.2 Validation Against Previous Work

4.2.1 Simulation Parameters

The present model will be validated against the experimental and numerical work of dry process introduced in Muhammad et al., 2013 using the same material and laser properties in addition to absorptivity of 85%. Moreover, the particle size, in Muhammad et al., 2013 of 5 μm, will result in discretizing the domain into 341 particles (11×31) in the present model. The simulation is done on PC with Intel Core i7 @ 2.50GHz and 8GB RAM, while its results compared with each other in terms of CPU time, bottom surface hole radius (denoted by exit radius), the percentage of removed volume by assuming the the total volume to be removed is the cylinder of radius r_b and metal thickness height.

For MLPG, both MLS and WLS will be used in locally approximating the temperature field in the present model for each weight function, quadratic and cubic polynomial bases, and different support domain radii. In case of RPIM, the condition number of matrix $\mathbf{R}$ is an indication of the solution accuracy and stability, so it will be calculated at a test particle in the center of the processed domain at the first time step. Monitoring of condition number will give a clear idea about its dependence on the increase/decrease in support domain neighboring particles in addition to the shape parameter value. Table 4.1 shows the material properties and laser beam parameters, while Table 4.2 shows the domain characteristics and simulation parameters.

Table 4.1: Thermo-physical properties of stainless steel 316L (Muhammad, Rogers, & Li, 2013)

Density	7950	$\mathrm{kg\,m^{-3}}$
Specific heat	470	$\mathrm{J\,kg^{-1}\,K^{-1}}$
Thermal conductivity	20	$\mathrm{W\,m^{-1}\,K^{-1}}$
Coefficient of heat convection	20	$\mathrm{W\,m^{-2}\,K^{-1}}$
Melting temperature	1723	K

Table 4.2: Domain characteristics and simulation parameters

Ambient temperature	300	K
Initial temperature	300	K
Domain dimensions	50×150	$\mu\mathrm{m}^2$
Number of particles	341	
Laser absorptivity	0.85	
Laser power	100	W
Beam radius at focal point	25	$\mu\mathrm{m}$
Time step	0.10	$\mu\mathrm{s}$
Total simulation time	150	$\mu\mathrm{s}$

4.2.2 Simulation Results

In Figure 4.1, the experimental work was conducted by applying a single pulse laser for three different pulse durations ($t = \{50, 100, 150\}$ μs). On the other hand, for the simulation results, results of MLPG are listed in Tables 4.3 to 4.8 for different weight functions, support domain radii, and quadratic ($m = 6$) and cubic ($m = 10$) polynomial bases, while for those of RPIM, Tables 4.9 and 4.10 show the results for different values of shape parameters α_m and α_e, and support domain radius h in both cases of MQ-RBF ($q = 1.03$) and EXP-RBF. Finally, for SSPH, Table 4.11 shows the results given from two different smoothing length values $h = \{1.2\Delta, 1.5\Delta\}$ and the three aforementioned kernel functions.

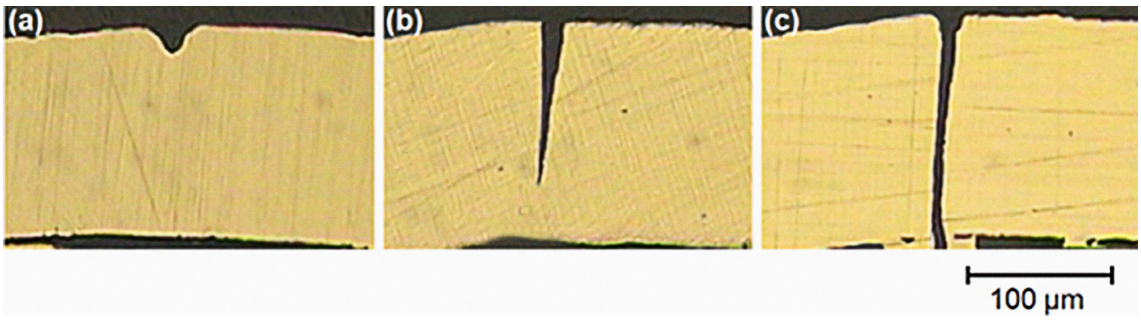

Figure 4.1: Experimental penetration depth at different single pulse durations (a) $t = 50$ μs, (b) $t = 100$ μs and (c) $t = 150$ μs (Muhammad, Rogers, & Li, 2013)

4.2.3 MLPG Simulation Results

For the present model, both MLS and WLS show high sensitivity to the choice of weight function, polynomial basis, and support domain radius. This sensitivity leads to the simulation failure several times (blank cells in Tables 4.3 to 4.8). This model sensitivity may be alleviated by employing the local weak form, considering other weight functions, or addressing other basis functions, however, this will not be investigated in the present work.

The best results, in terms of removed volume and exit radius, can be obtained using MLS by choosing cubic spline weight function, cubic polynomial basis, and support radius $h = 3.5\Delta$ as given in Table 4.4. Similarly, for WLS, the best results can be given by choosing Gaussian weight function, cubic polynomial basis, and support radius $h = 3.1\Delta$ as given in Table 4.8. In either case, both removed volume and bottom surface radius are the same. However, WLS outperforms MLS in terms of computational load, since the calculations of shape functions spatial derivatives are more computationally expensive in case of MLS as comparatively seen in Equation (3.18) and Equation (3.29).

As previously said, the global compatibility of MLS is not an issue in case of collocation method, which makes WLS the best choice for its comparatively dramatic rection in CPU time (55.92%). Therefore, the simulation results of WLS using Gaussian weight function, cubic polynomial basis, and support radius $h = 3.1\Delta$ is considered to be the most optimum choice.

Table 4.3: Cubic spline weight function with quadratic polynomial basis

			h=2Δ	h=2.1Δ	h=2.5Δ	h=2.9Δ	h=3Δ
MLS	CPU Time	s	—	235	322	401	460
	Exit Radius	μm	—	7.50	7.50	2.50	2.50
	Removed Volume	%	—	77.33	74.67	71	69.67
WLS	CPU Time	s	—	—	192	230	261
	Exit Radius	μm	—	—	2.50	2.50	2.50
	Removed Volume	%	—	—	68.33	66.33	65.67

Table 4.4: Cubic spline weight function and cubic polynomial basis

			h=3Δ	h=3.1Δ	h=3.5Δ	h=3.9Δ	h=4Δ
MLS	CPU Time	s	—	463	574	673	726
	Exit Radius	μm	—	7.50	12.50	7.50	7.50
	Removed Volume	%	—	79.33	79.67	78	78
WLS	CPU Time	s	—	—	319	378	403
	Exit Radius	μm	—	—	12.50	7.50	7.50
	Removed Volume	%	—	—	78.33	76.67	77.33

4.2.4 RPIM Simulation Results

It can be seen from Tables 4.9 and 4.10 that both MQ-RBF and EXP-RBF give nearly the same results in terms of exit radius and percentage of removed metal volume. However, EXP-RBF greatly outperforms MQ-RBF from the computational load point of view with significant reduction of CPU time around 25% to 40%. However, for the matrix $\mathbf{R}$ condition number, EXP-RBF results in constructing $\mathbf{R}$ with huge condition number compared to MQ-RBF especially for low values of α_e. Additionally, the increase in support domain particles number (higher h) leads to a significantly higher condition number of $\mathbf{R}$ which may deteriorate the solution accuracy and stability, if numerous number of neighboring particles is injudiciously chosen.

As seen in the first column of Table 4.10 where $\alpha_e = 0.003$ and $h = 4\Delta$, $\mathbf{R}$ condition

Table 4.5: Quartic spline weight function and quadratic polynomial basis

			h=2Δ	h=2.1Δ	h=2.5Δ	h=2.9Δ	h=3Δ
MLS	CPU Time	s	243	223	—	—	—
	Exit Radius	μm	7.50	7.50	—	—	—
	Removed Volume	%	76.67	76	—	—	—
WLS	CPU Time	s	137	—	205	225	263
	Exit Radius	μm	7	—	2.50	2.50	2.50
	Removed Volume	%	76	—	66.33	65.67	65.67

Table 4.6: Quartic spline weight function and cubic polynomial basis

			h=3Δ	h=3.1Δ	h=3.5Δ	h=3.9Δ	h=4Δ
MLS	CPU Time	s	—	—	—	—	—
	Exit Radius	μm	—	—	—	—	—
	Removed Volume	%	—	—	—	—	—
WLS	CPU Time	s	—	—	332	391	399
	Exit Radius	μm	—	—	7.50	7.50	7.50
	Removed Volume	%	—	—	78	76.67	75.33

number is too high that the simulation stopped after a few time steps due to the aggressive solution instability driven by the massive condition number which supports the foregoing discussion in Section 3.3.2. Generally speaking, for the present problem, EXP-RBF can be chosen as the best selection of RBF (in terms of CPU time and removed volume percentage) with shape parameter $\alpha_e = 0.03$ and $h = 2\Delta$.

4.2.5 SSPH Simulation Results

It can be seen that the three kernel functions show slight deviation from each other, however, for the present case, the Cubic B-Spline with $l_s = 1.2\Delta$ gives the most accurate result compared with the experimental work in the shortest computational time.

According to the previous results, the three meshfree methods show nearly the same

Table 4.7: Gaussian weight function and quadratic polynomial basis

			h=2Δ	h=2.1Δ	h=2.5Δ	h=2.9Δ	h=3Δ
MLS	CPU Time	s	—	—	313	393	442
	Exit Radius	μm	—	—	12.50	12.50	7.50
	Removed Volume	%	—	—	78.33	77.67	76
WLS	CPU Time	s	—	—	197	223	249
	Exit Radius	μm	—	—	2.50	2.50	2.50
	Removed Volume	%	—	—	69.67	67	67

Table 4.8: Gaussian weight function and cubic polynomial basis

			h=3Δ	h=3.1Δ	h=3.5Δ	h=3.9Δ	h=4Δ
MLS	CPU Time	s	—	—	574	674	—
	Exit Radius	μm	—	—	12.50	12.50	—
	Removed Volume	%	—	—	77.67	77.67	—
WLS	CPU Time	s	—	253	313	361	396
	Exit Radius	μm	—	12.50	12.50	7.50	7.50
	Removed Volume	%	—	79.67	78.33	76.67	76.67

agreement with the previous numerical and experimental work in terms of drilled hole geometry. However, for computation efficiency, SSPH is superior for its significantly low CPU time 72 s compared to 253 s for MLPG (WLS) and 114 s for RPIM (EXP-RBF). Therefore, in the present work, SSPH is optimally chosen to be used in this meshfree model of metal laser drilling for its efficient computing aspect.

4.2.6 Effect of Support Radius Length

It is worth noting that unnecessarily long support radius deteriorates the solution accuracy and degrades the computational efficiency. On one hand, for solution accuracy, unnecessarily higher number of neighboring particles leads to suppressing the laser high temperature gradient by including the further particles with lower temperatures. On the other hand, for computational efficiency, more neighboring particles means bigger-sized

Table 4.9: Simulation results for MQ-RBF shape parameter $\alpha_m = \{3, 4, 5, 6\}$

			$\alpha_m = 3$	$\alpha_m = 4$	$\alpha_m = 5$	$\alpha_m = 6$
h=2Δ	CPU Time	s	152	157	151	158
	Exit Radius	μm	12.50	12.50	12.50	12.50
	Removed Volume	%	78.33	78.33	78.33	77.67
	Condition Number ($\mathbf{R}$)	$\times 10^6$	0.33	1.70	7.14	24.86
h=3Δ	CPU Time	s	227	227	225	231
	Exit Radius	μm	12.50	12.50	12.50	12.50
	Removed Volume	%	78.33	78.33	77.67	77.67
	Condition Number ($\mathbf{R}$)	$\times 10^7$	0.27	2.18	14.44	78.70
h=4Δ	CPU Time	s	291	301	295	304
	Exit Radius	μm	12.50	12.50	12.50	12.50
	Removed Volume	%	78.33	77.67	77	77
	Condition Number ($\mathbf{R}$)	$\times 10^8$	0.09	0.97	8.90	68.34

Table 4.10: Simulation results for EXP-RBF shape parameter $\alpha_e = \{0.003, 0.01, 0.02, 0.03\}$

			$\alpha_e = 0.003$	$\alpha_e = 0.01$	$\alpha_e = 0.02$	$\alpha_e = 0.03$
h=2Δ	CPU Time	s	113	108	113	114
	Exit Radius	μm	12.50	12.50	12.50	12.50
	Removed Volume	%	77.67	77.67	77.67	78.33
	Condition Number ($\mathbf{R}$)	$\times 10^8$	303	2.40	0.15	0.03
h=3Δ	CPU Time	s	147	145	149	153
	Exit Radius	μm	7.50	7.50	12.50	12.50
	Removed Volume	%	76	67	77	77
	Condition Number ($\mathbf{R}$)	$\times 10^{12}$	503	0.3480	0.0050	0.0004
h=4Δ	CPU Time	s	—	180	177	180
	Exit Radius	μm	—	7.50	7.50	7.50
	Removed Volume	%	—	76	76	76
	Condition Number ($\mathbf{R}$)	$\times 10^{14}$	2420	2.60	0.009	0.0003

Table 4.11: SSPH simulation results for different values of smoothing length and kernel functions

			Cubic B-Spline	Revised Super Gauss	Quartic
$l_s = 1.2\Delta$	Computational Time	s	72	82	73
	Exit Radius	μm	12.50	12.50	7.50
	Removed Volume	%	77	77	75.33
$l_s = 1.5\Delta$	Computational Time	s	103	94	93
	Exit Radius	μm	2.50	2.50	2.50
	Removed Volume	%	67	70.33	65.67

local matrices and vectors for calculating the shape functions in addition to the decrease in number of zeros elements in the global matrices, which means more memory has to be allocated for more calculations to be carried out.

4.2.7 Estimation of Penetration Depth

Figure 4.2 shows the drilled metal penetration depth at the same irradiation processing time of those used in the experimental work $t = \{50, 100, 150\}$ μs. In Figure 4.1, laser drilling exhibits full penetration by the end of the processing time $t = 150$ μs. On the other hand, for the same processing time, the present model shows partial penetration as depicted in Figure 4.2. This deviation from the experimental data can be attributed to the model assumptions of fixing the laser absorptivity value, molten pool hydrodynamics and pressurized assist gas effect.

In Figure 4.3, the present model penetration depth is graphed with the experimental and numerical ones from Muhammad et al., 2013. It can be noted that the experimental penetration depth exponentially develops with time because of higher laser absorptivity at deeper holes and higher temperature. The experimental data, before reaching full-depth penetration, is interpolated (as depicted by green dashed line, Expr. Intp., in Figure 4.3) to give clear insight into the exponential behavior shown by penetration depth development. Consequently, the present numerically calculated depth reaches the

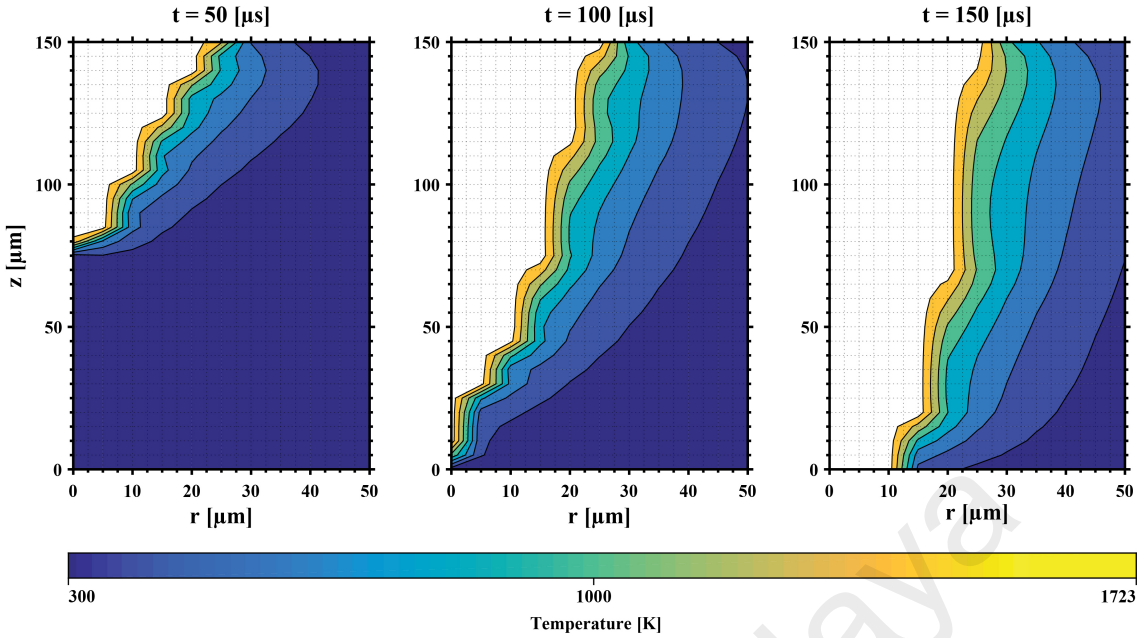

Figure 4.2: Transient development of the hole penetration depth

bottom surface at nearly the same time as the interpolated experimental data exhibits, which shows the good accuracy of simulation results.

4.2.8 Variation of Laser Absorption

For the experimental work in Figure 4.3, the metal is removed at slow rate in the early stage (i.e. $t = [0, 50]$ μs). This slow rate comes mainly from the low absorptivity at low temperature and depth. However, later on, the depth develops exponentially with time due to the abrupt increase in absorptivity with higher temperature and deeper depth (Bergström, 2008). In particular, stainless steel laser absorptivity can lie in the range $\alpha_l = [35\%, 56\%]$ according to the surface texture/roughness (Bergström, Powell, & Kaplan, 2007).

To shed the light on the impact of laser absorptivity variation on the ablation pace, an arbitrary value of $\alpha_l = 40\%$ will be tested to account for laser ablation at room temperature and compared with the first experimental set of laser pulse $t = [0, 50]$ μs. The simulation result in Figure 4.4 shows very good agreement with the experimental data where the penetration depth is monitored and plotted every 5 μs. This proves that the laser absorptivity has low value in the early processing time of laser ablation, while it abruptly increases with time because of higher temperature and depth. For more

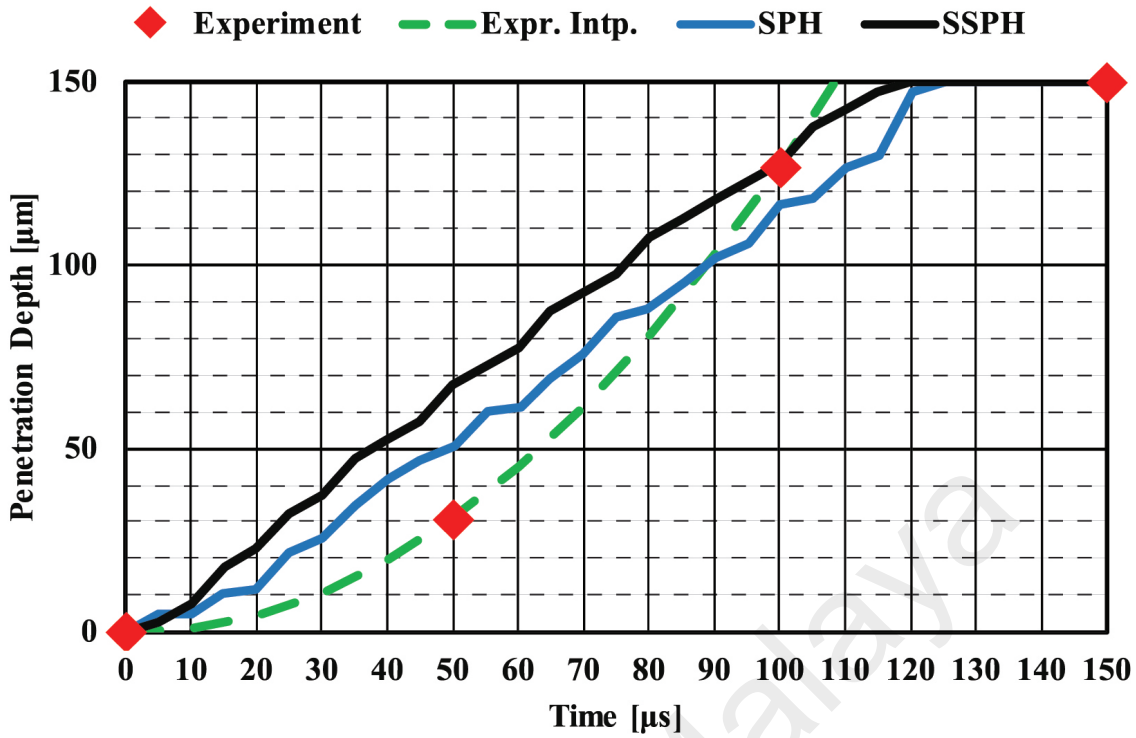

Figure 4.3: Numerically calculated penetration depth (SPH (Muhammad, Rogers, & Li, 2013) and SSPH) with experimental work (Muhammad, Rogers, & Li, 2013) and its interpolation

simulation accuracy over the whole processing time, the laser absorptivity can be formulated as a function of penetration depth, metal temperature, laser beam multiple hole reflections, and the molten pool hydrodynamics.

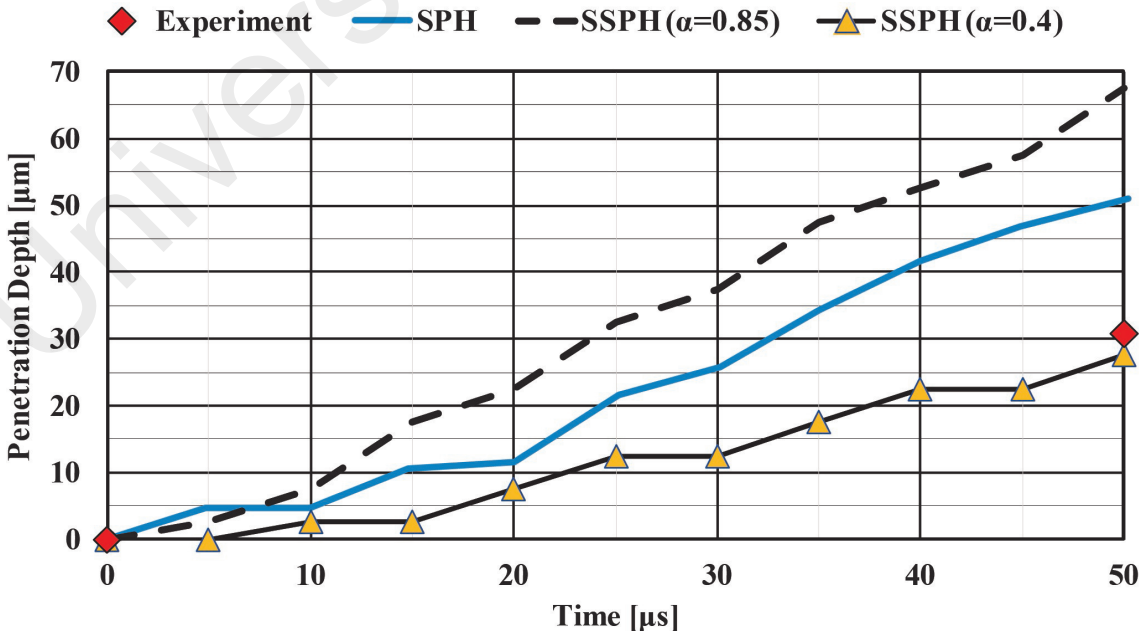

Figure 4.4: SSPH numerical result of absorptivity $\alpha_l = 0.4$ against experimental and numerical work of SPH and SSPH($\alpha_l = 0.85$) for $t = [0, 50]$ µs

Table 4.12: Thermo-physical properties of SS304 and AA5083 (Dowden, 2001; Achebo & Oghoore, 2012; Ezazi, Yusof, Sarhan, Shukor, & Fadzil, 2015)

		SS304	AA5083
Density	$[\mathrm{kg\,m^{-3}}]$	7900	2650
Specific heat	$[\mathrm{J\,kg^{-1}\,K^{-1}}]$	450	900
Thermal conductivity	$[\mathrm{W\,m^{-1}\,K^{-1}}]$	15	120
Melting temperature	[K]	1698	850

4.3 Validation Against Experimental Data

4.3.1 Experimental Setup

In order to further verify the model accuracy, a set of experiments is conducted on two thin sheets of stainless steel SS304 and one thin sheet of aluminum alloy AA5083, and Table 4.12 shows the thermo-physical properties of both metals.

The experiments are conducted to validate the model estimation of penetration time. In order to do this, two photocells are mounted on the top and bottom surfaces of each sheet. The machine operator arbitrarily chooses a drilling time sufficient for laser beam to penetrate the bottom surface without necessitating a full penetration since the comparison between the experimental data and the numerical results is done in terms of the time required for the laser beam to merely penetrate the bottom surface without paying attention to the final hole profile/geometry. Both photocells are illuminated by the laser beam hitting the top surface and penetrating the bottom surface, while the output analog voltages of photocells are monitored and saved by an oscilloscope as depicted in Figure 4.5. On the other hand, the metal sheets are used in their as-received state.

The experiments are conducted on a CW CO_2 laser machine *LVD Axel 3015 S* shown in Figure 4.6, while the experiments parameters are given in Table 4.13. The machine always guarantees that the focal radius lies on the irradiated metal top surface, which increases the quality of the drilling by eliminating the effect of beam defocusing. Different levels of

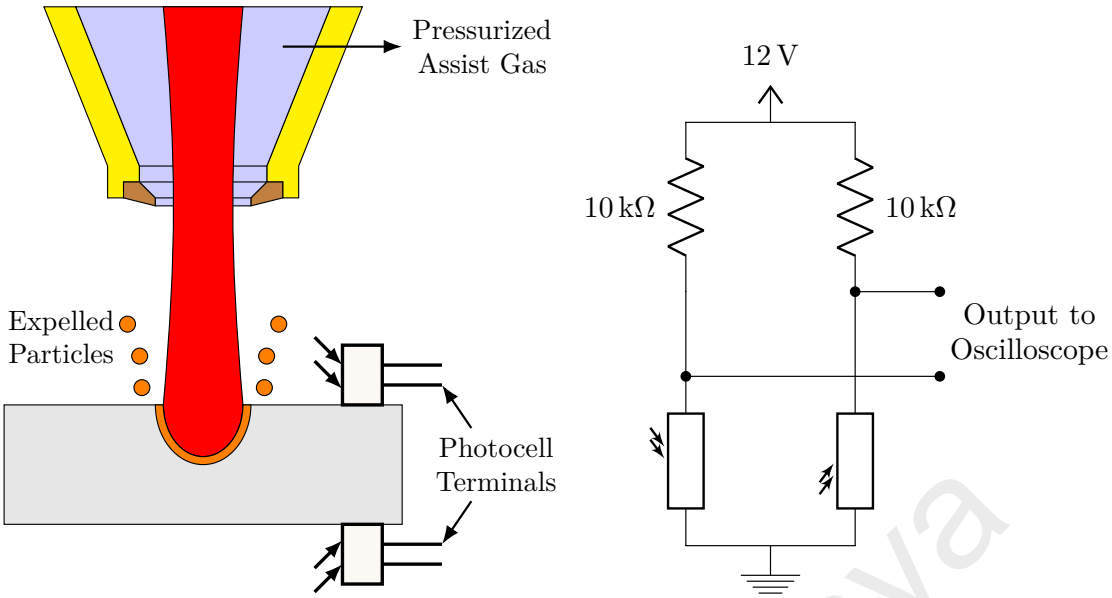

(a) Experimental setup (b) Photocells circuit schematic

Figure 4.5: Schematic of experimental setup and photocells circuit

Figure 4.6: Industrial CO_2 laser machine (LVD Axel 3015 S) used in the experiments

laser power are used, and for each level of laser power, a set of three experiments is done in order to make sure of the experimental reproducibility. Highly pressurized Nitrogen assist gas is used to make sure that the metal particles are immediately expelled once they are melted.

4.3.2 Experimental Data

Figures 4.7 to 4.9 show the output voltages of top surface photocell (V_T) and bottom surface photocell (V_B) for the metal sheets and laser powers as given in Table 4.13, and penetration time t_p is illustrated in each graph. Figures 4.7(a) to 4.7(c), Figures 4.8(a) to 4.8(c) and Figures 4.9(a) to 4.9(c) show the output voltages for the three experiments done for the sake of ensuring the experimental reproducibility for any given sheet and

Table 4.13: Experiments parameters for metal sheets of SS304 and AA5083

		SS304		AA5083
Thickness	[µm]	500	1000	1000
Power Levels	[W]	1500	1500	2500
Focal Radius	[µm]		150	
Assist Gas Pressure	[bar]		10	

laser power. Top and bottom surfaces of the holes are depicted in Figures 4.10 to 4.12 and Figures 4.13 to 4.15, respectively.

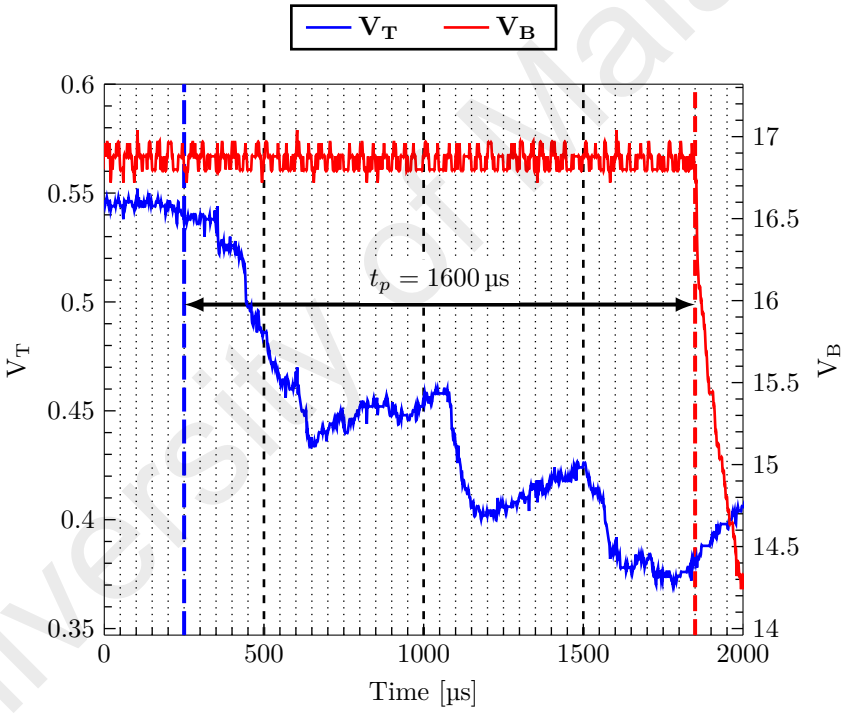

Figure 4.7(a)

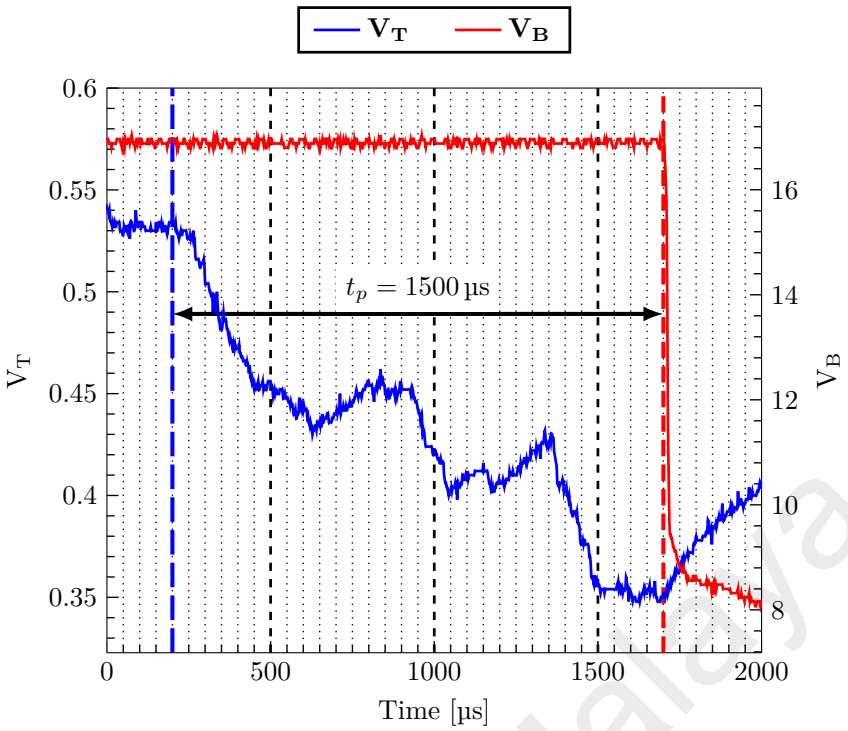

Figure 4.7(b)

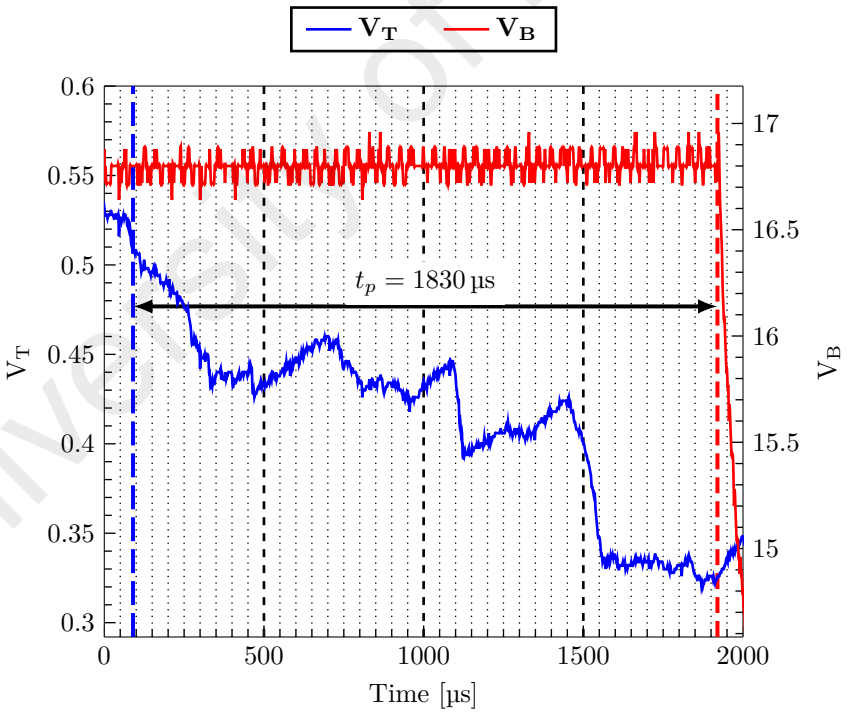

Figure 4.7(c)

Figure 4.7: Output voltages for 500 µm thick SS304 sheet and 1500 W laser power

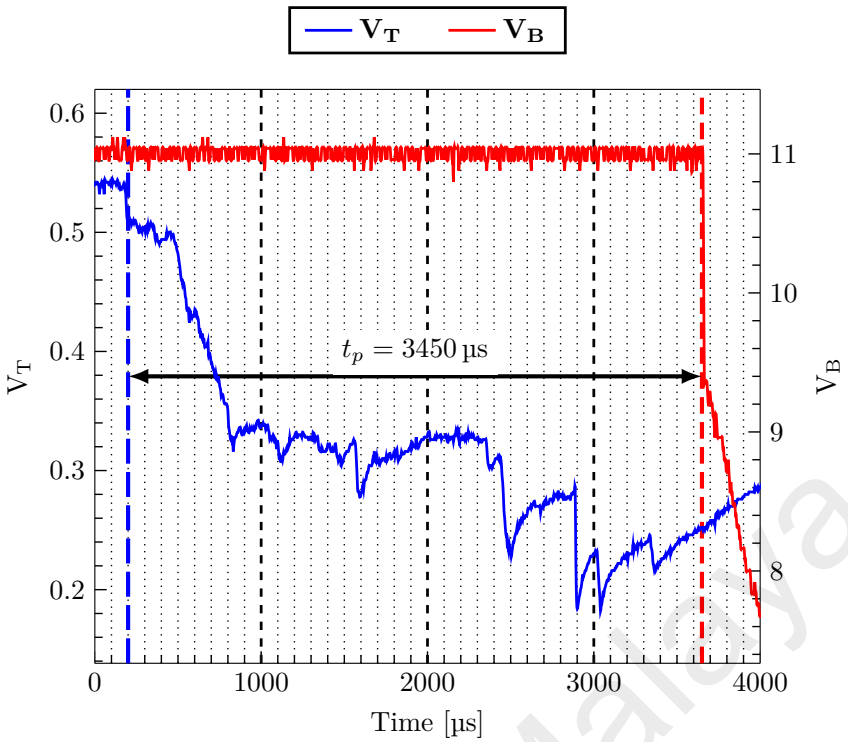

Figure 4.8(a)

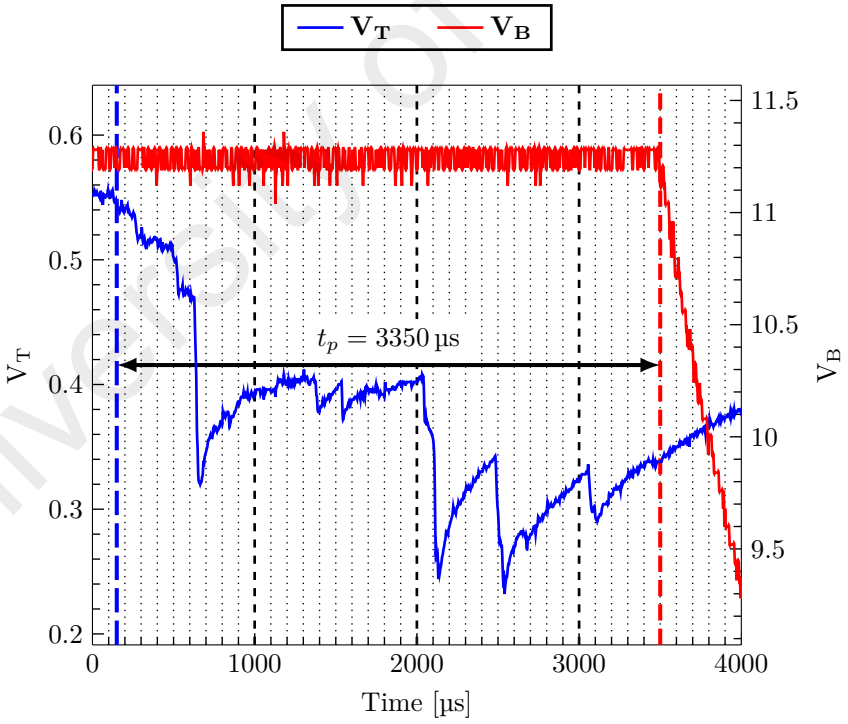

Figure 4.8(b)

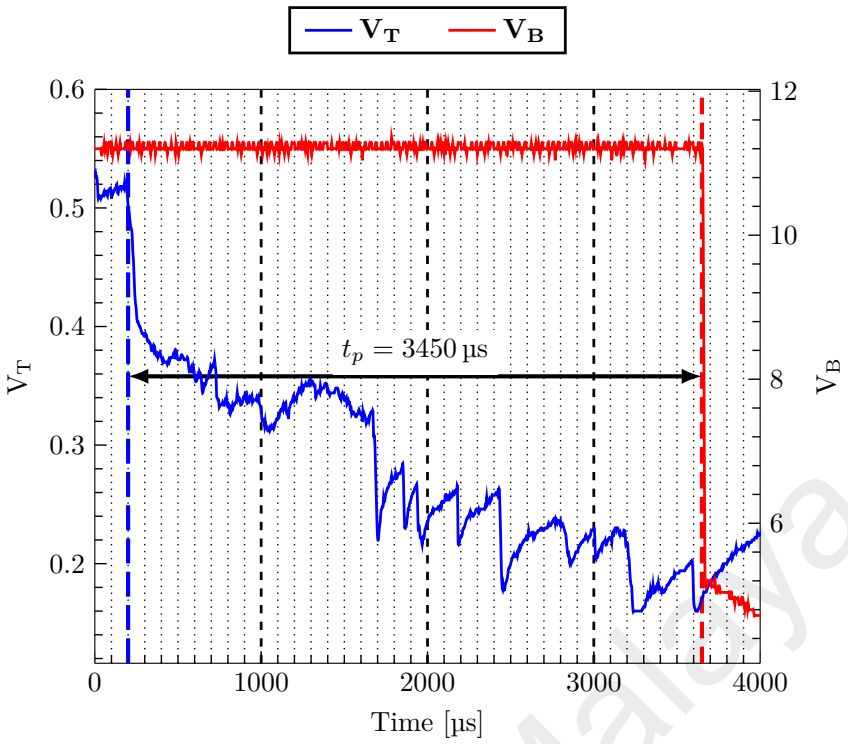

Figure 4.8(c)

Figure 4.8: Output voltages for 1000 μm thick SS304 sheet and 1500 W laser power

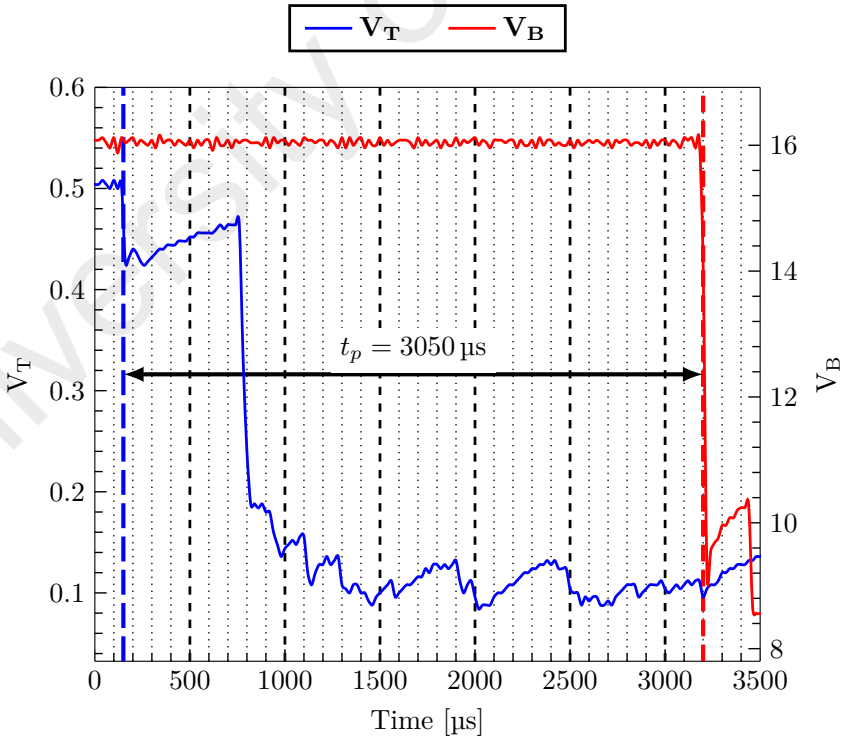

Figure 4.9(a)

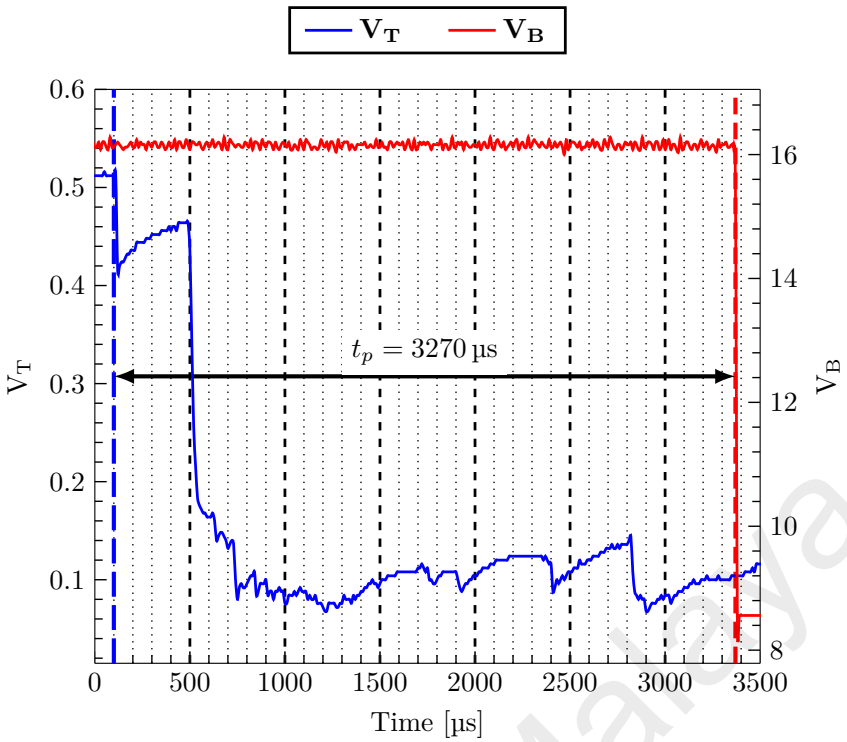

Figure 4.9(b)

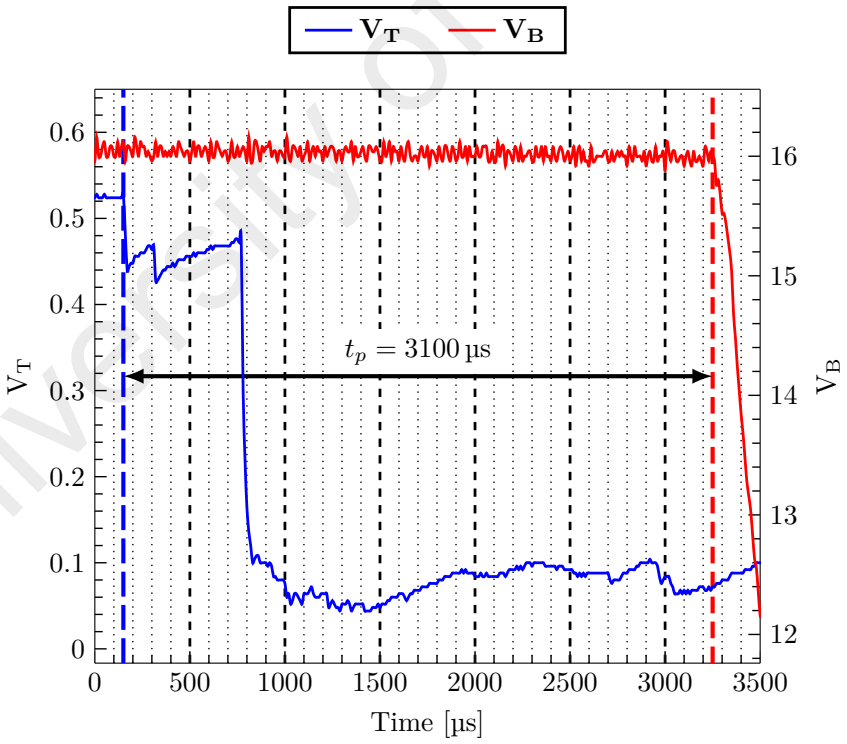

Figure 4.9(c)

Figure 4.9: Output voltages for 1000 µm thick AA5083 sheet and 2500 W laser power

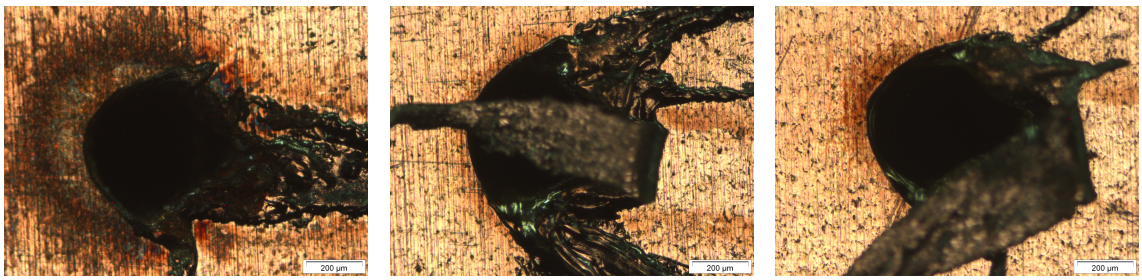

(a) (b) (c)

Figure 4.10: Holes top surfaces of 500 μm SS304 sheet

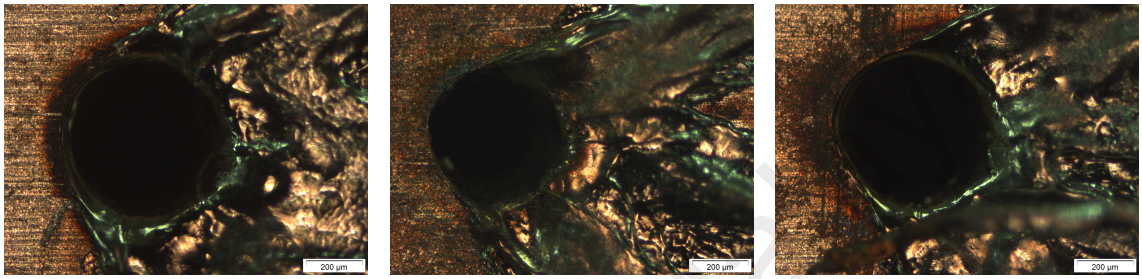

(a) (b) (c)

Figure 4.11: Holes top surfaces of 1000 μm SS304 sheet

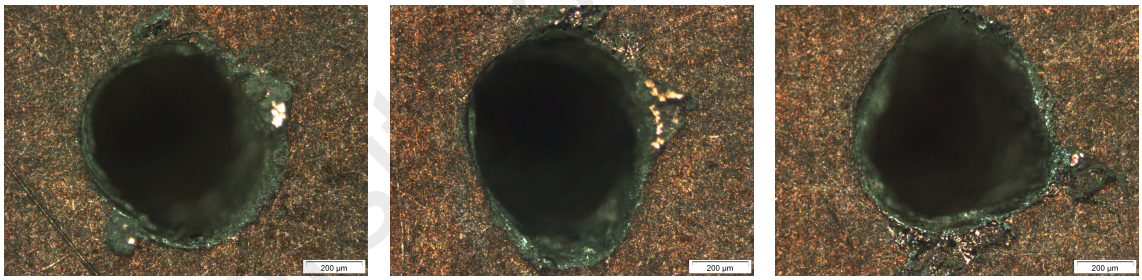

(a) (b) (c)

Figure 4.12: Holes top surfaces of 1000 μm AA5083 sheet

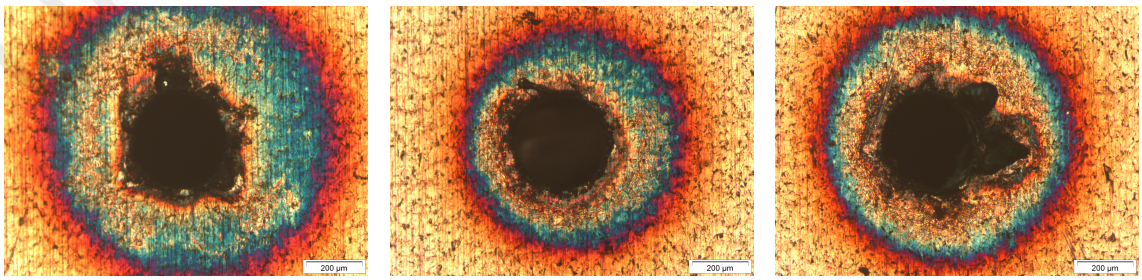

(a) (b) (c)

Figure 4.13: Holes bottom surfaces of 500 μm SS304 sheet

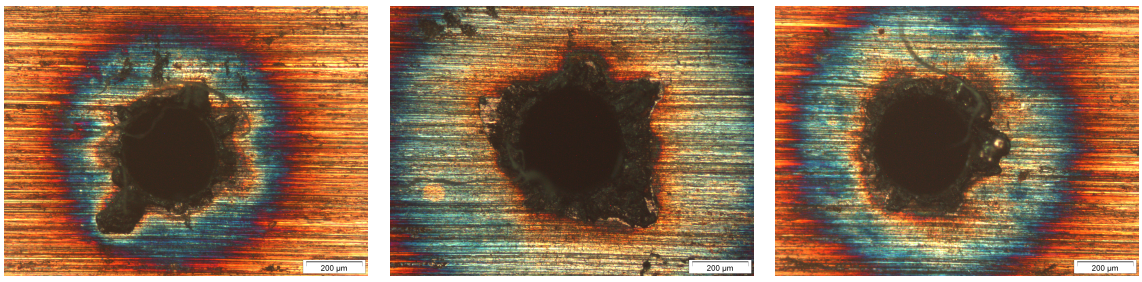

(a) (b) (c)

Figure 4.14: Holes bottom surfaces of 1000 μm SS304 sheet

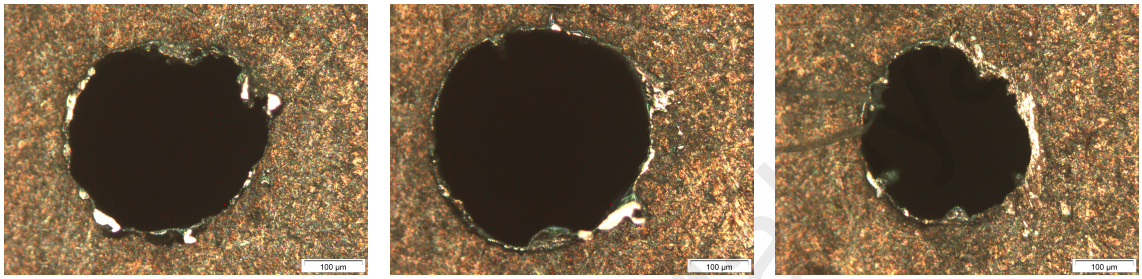

(a) (b) (c)

Figure 4.15: Holes bottom surfaces of 1000 μm AA5083 sheet

In Figures 4.10 to 4.12, compared to aluminum, all the top surfaces of stainless steel sheets have a significant amount of spatter proportional to the incident laser power, which can be attributed to the higher boiling temperature and viscosity in addition to the lower laser power which wasn't sufficient to significantly evaporate some molten metal. This significant accumulation of spatter during the ablation led to the remarkable fluctuations of the top surface photocell output voltage V_T, as shown in Figures 4.7 and 4.8, since the spatter accumulated in the midway between the photocell and the hole center, and caused some scatter, reflection and/or obscuration of the laser beam before reaching the photocell. However, on the other hand, the dross-free bottom surfaces, as shown in Figures 4.13 to 4.15, made the output voltage of bottom surface photocell, V_B in Figures 4.7 and 4.8, change almost monotonically without these significant fluctuations. It is noteworthy that there is some difference in the penetration time between one experiment and another, and it may be a result of the existence of some surface contamination in addition to unavoidably inhomogeneous surface roughness and microstructure over the metal sheet.

Table 4.14: Domain characteristics and simulation parameters

		SS304	AA5083
Ambient temperature	[K]	300	
Initial temperature	[K]	300	
Domain width	[μm]	300	1000
Number of particles in radial direction		25	27
Particle size	[μm]	12.50	38.46
Focal radius	[μm]	150	
Time step	[μs]	1	0.50

Table 4.15: Penetration time t_p in [μs] for the experimental data and simulation results

	SS304		AA5083
Thickness [μm]	500	1000	1000
First Experiment	1600	3450	3050
Second Experiment	1500	3350	3270
Third Experiment	1830	3450	3100
Simulation Results	1605	3205	3235

4.3.3 Simulation Results

SSPH is used for simulation using the same properties and parameters of both metal sheets and laser beam of every experiment in Table 4.13. Simulation parameters are given in Table 4.14. Both experimental data and model results are compared with each other in terms of penetration time as given in Table 4.15. For laser absorptivity of SS304, as previously discussed, a value of $\alpha_l = 85\%$ is used. On the other hand for aluminum alloys, the absorptivity is generally known to be very low. Therefore, a value of $\alpha_l = 15\%$ is arbitrarily taken for AA5083 to be higher than that of **??** in order to account for the high surface temperature and multiple beam reflections against the keyhole walls.

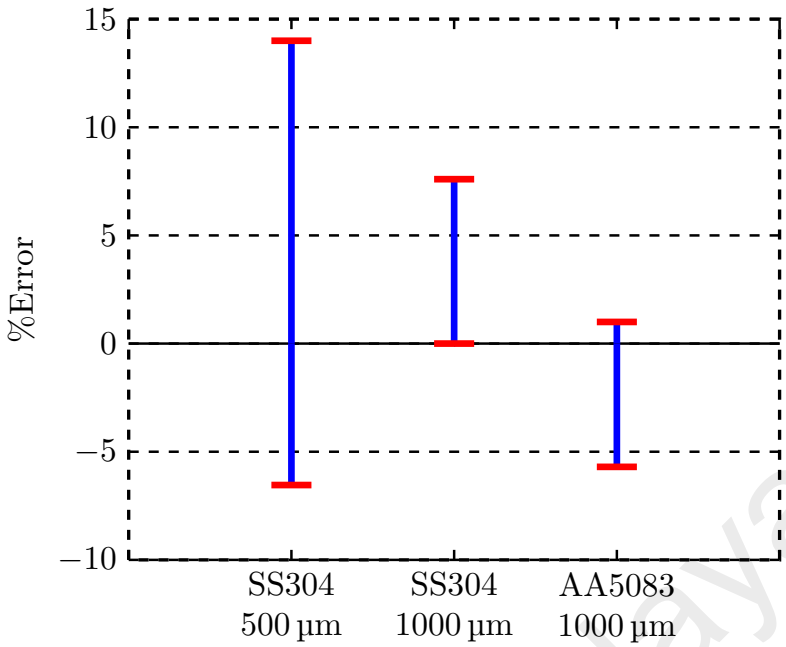

Figure 4.16: Percent error of the predicted penetration time t_p

The percent error of the predicted penetration time is given by

$$\%Error = \frac{Experimental - Simulation}{Simulation} \times 100 \tag{4.1}$$

and shown in Figure 4.16 for all sheets of SS304 and AA5083. Accordingly, it can be seen that present model shows good agreement with the experimental data of different thicknesses and metals. This can prove the model robustness and potential for further improvements to simulate as closely as possible the physically complex process of metal laser drilling.

CHAPTER 5: CONCLUSION AND FUTURE RECOMMENDATIONS

5.1 Conclusion

In the present work, a simplified numerical model was built for simulating the metal removal in laser drilling using meshfree collocation methods in order to overcome the difficulties faced by mesh-based methods when handling such problems of severe deformation and domain separation. The model results were compared with a relevant meshfree published work in addition to a set of experimental data. Three different meshfree methods, (meshless local Petrov-Galerkin (MLPG), symmetric smoothed particle hydrodynamics (SSPH) and radial point interpolation method (RPIM)) were considered and compared with each other in terms of the prediction of penetration depth and hole geometry.

For MLPG, both moving least square (MLS) and weighted least square (WLS) were used for approximating the temperature field. WLS showed its advantage of significantly lower computational time without substantial superiority for MLS due to the used collocation method. Additionally, MLPG showed instability and high sensitivity to the support domain radius value, which needs further investigation. RPIM with its dimensionality-independence did show also dramatic reduction in computational load compared to MLPG with the same predicted hole geometry. For SSPH, the simulation computation load was dramatically reduced in comparison with MLPG. The prediction of hole geometry was almost the same as that of MLPG. Considering the CPU time of both SSPH and RPIM, SSPH managed to significantly reduce the CPU time by 36%, which made it the optimal method for the present model in terms of computational efficiency.

When validated against a relevant meshfree published work, the model results showed the significant impact of the estimation of laser absorptivity on the prediction of

penetration depth and hole geometry. For the present work considering thin metal sheets, the approximation of laser absorptivity to be a constant value led to a good agreement with the experimental data especially when the target metal is heated up with the formation of molten pool. However, in the early stage of drilling, the absorptivity is low and responsive to the temperature rise.

A set of experiments was conducted to further validate the model accuracy of predicting the penetration time. Two thicknesses of thin stainless steel sheets and one thin aluminum sheet are used for experimental validation. The experiments were repeated three times to ensure the reproducibility. The model prediction of penetration time was in good agreement with the experiments data.

In addition to the construction and validation of the present model, it was turned into a standalone application. This standalone application can be easily integrated into a graphical user interface (GUI) of an industrial laser machine since it is lightweight and not computationally expensive for such problems.

5.2 Recommendations for Future Work

The present model with its assumptions shows good agreement with the experimental data in case of thin metal sheets. However, this work can be extended in several ways in order to get as close as possible to the physical complexity of metal laser drilling:

- Laser abosprtivity should be modeled to account for the progress of the keyhole front and the target metal temperature.
- Molten pool hydrodynamics should be considered especially when the metal is thick and/or the assist gas pressure is not high enough to effectively expel the molten particles.
- The choice of particle size needs to be investigated and treated as a function of the target metal thermo-physical properties and metallurgy.

- Thermal deformation and stresses have to be considered and modeled for thick sheets.
- Plasma formation is inevitable for high laser power in the absence of assist gas pressure. Therefore, its shield should be modeled to properly estimate the amount of laser energy hitting the target metal irradiated surface.

REFERENCES

Achebo, J. I. & Oghoore, O. (2012). Numerical computation of melting efficiency of aluminum alloy 5083 during CO2 laser welding process. In *Materials with complex behaviour II* (Vol. 16, pp. 601–617). Springer Nature.

Ahmadi, I., Sheikhy, N., Aghdam, M., & Nourazar, S. (2010). A new local meshless method for steady-state heat conduction in heterogeneous materials. *Engineering Analysis with Boundary Elements*, *34*(12), 1105–1112.

Akarapu, R., Li, B. Q., & Segall, A. (2004). A thermal stress and failure model for laser cutting and forming operations. *Journal of Failure Analysis and Prevention*, *4*(5), 51–62.

Arif, A., Yilbas, B., & Aleem, B. A. (2009). Laser cutting of thick sheet metals: Residual stress analysis. *Optics & Laser Technology*, *41*(3), 224–232.

Atluri, S. N., Kim, H.-G., & Cho, J. Y. (1999). A critical assessment of the truly meshless local petrov-galerkin (mlpg), and local boundary integral equation (lbie) methods. *Computational Mechanics*, *24*(5), 348–372.

Atluri, S. N. & Zhu, T. (1998). A new meshless local petrov-galerkin (MLPG) approach in computational mechanics. *Computational Mechanics*, *22*(2), 117–127.

Atluri, S. N. (2004). *The meshless method (mlpg) for domain & bie discretizations*. Tech Science Press Forsyth.

Batra, R. C. & Zhang, G. M. (2007). SSPH basis functions for meshless methods, and comparison of solutions with strong and weak formulations. *Computational Mechanics*, *41*(4), 527–545.

Belytschko, T., Lu, Y. Y., & Gu, L. (1994). Element-free galerkin methods. *International Journal for Numerical Methods in Engineering*, *37*(2), 229–256.

Bergström, D., Powell, J., & Kaplan, A. (2007). The absorptance of steels to nd:YLF and nd:YAG laser light at room temperature. *Applied Surface Science*, *253*(11), 5017–5028.

Bergström, D. (2008). *The Absorption of Laser Light by Rough Metal Surfaces* (Doctoral dissertation, Luleå University of Technology).

Calamaz, M., Limido, J., Nouari, M., Espinosa, C., Coupard, D., Salaün, M., … Chieragatti, R. (2009). Toward a better understanding of tool wear effect through a comparison between experiments and SPH numerical modelling of machining hard materials. *International Journal of Refractory Metals and Hard Materials*, *27*(3), 595–604.

Campbell, J., Vignjevic, R., & Patel, M. H. (2008). A coupled FE-SPH pproach for simulation of structural response to extreme wave and green water loading. In *Offshore technology conference* (19429-MS). Society of Petroleum Engineers (SPE).

Chan, C. L. & Mazumder, J. (1987). One-dimensional steady-state model for damage by vaporization and liquid expulsion due to laser-material interaction. *Journal of Applied Physics*, *62*(11), 4579.

Chang, T.-J., Kao, H.-M., Chang, K.-H., & Hsu, M.-H. (2011). Numerical simulation of shallow-water dam break flows in open channels using smoothed particle hydrodynamics. *Journal of Hydrology*, *408*(1-2), 78–90.

Chen, J. K., Beraun, J. E., & Carney, T. C. (1999). A corrective smoothed particle method for boundary value problems in heat conduction. *International Journal for Numerical Methods in Engineering*, *46*(2), 231–252.

Chen, W., Fu, Z.-J., & Chen, C. (2014). *Recent advances in radial basis function collocation methods*. SpringerBriefs in Applied Sciences and Technology. Springer Berlin Heidelberg.

Cheng, C., Tsui, Y., & Clyne, T. (1998). Application of a three-dimensional heat flow model to treat laser drilling of carbon fibre composites. *Acta Materialia*, *46*(12), 4273–4285.

Cheng, A.-D. (2012). Multiquadric and its shape parameter—a numerical investigation of error estimate, condition number, and round-off error by arbitrary precision computation. *Engineering Analysis with Boundary Elements*, *36*(2), 220–239.

Cleary, P. W. & Monaghan, J. J. (1999). Conduction modelling using smoothed particle hydrodynamics. *Journal of Computational Physics*, *148*(1), 227–264.

Collins, J. & Gremaud, P. (2011). A simple model for laser drilling. *Mathematics and Computers in Simulation*, *81*(8), 1541–1552.

Comas-Cardona, S., Groenenboom, P., Binetruy, C., & Krawczak, P. (2005). A generic mixed FE-SPH method to address hydro-mechanical coupling in liquid composite moulding processes. *Composites Part A: Applied Science and Manufacturing*, *36*(7), 1004–1010.

Dai, B., Zheng, B., Liang, Q., & Wang, L. (2013). Numerical solution of transient heat conduction problems using improved meshless local petrov–galerkin method. *Applied Mathematics and Computation*, *219*(19), 10044–10052.

Dai, Y. J., Wu, X. H., & Tao, W. Q. (2011). Weighted least-squares collocation method (WLSCM) for 2-D and 3-D heat conduction problems in irregular domains. *Numerical Heat Transfer, Part B: Fundamentals*, *59*(6), 473–494.

Divo, E. A. & Kassab, A. J. (2014). A locally-integrated meshless (lim) method applied to advection-diffusion problems. In *International conference on heat transfer, fluid mechanics and thermodynamics*. Proceedings of the 10th International Conference on Heat Transfer, Fluid Mechanics and Thermodynamics.

Divo, E. & Kassab, A. J. (2007). An efficient localized radial basis function meshless method for fluid flow and conjugate heat transfer. *Journal of Heat Transfer*, *129*(2), 124.

Dowden, J. M. (2001). *The mathematics of thermal modeling: An introduction to the theory of laser material processing*. Chapman and Hall/CRC.

Dubey, A. K. & Yadava, V. (2008). Laser beam machining—a review. *International Journal of Machine Tools and Manufacture*, *48*(6), 609–628.

Espinosa, C., Lacome, J. L., Limido, J., Salaun, M., Mabru, C., & Chieragatti, R. (2008). Modeling high speed machining with the sph method. *10th International LS-DYNA users conference*, (3), 9–20.

Ezazi, M., Yusof, F., Sarhan, A. A., Shukor, M. H. A., & Fadzil, M. (2015). Employment of fiber laser technology to weld austenitic stainless steel 304l with aluminum alloy 5083 using pre-placed activating flux. *Materials & Design*, *87*, 105–123.

Fernández-Méndez, S., Bonet, J., & Huerta, A. (2005). Continuous blending of SPH with finite elements. *Computers & Structures*, *83*(17-18), 1448–1458.

Fornberg, B. & Piret, C. (2008). On choosing a radial basis function and a shape parameter when solving a convective pde on a sphere. *Journal of Computational Physics*, *227*(5), 2758–2780.

Fu, Z.-J., Chen, W., & Qin, Q.-H. (2012). Three boundary meshless methods for heat conduction analysis in nonlinear FGMs with kirchhoff and Laplace transformation. *Adv. Appl. Math. Mech. 4*(05), 519–542.

Ganesh, R. K., Bowley, W. W., Bellantone, R. R., & Hahn, Y. (1996). A model for laser hole drilling in metals. *Journal of Computational Physics*, *125*(1), 161–176.

Ganesh, R., Faghri, A., & Hahn, Y. (1997a). A generalized thermal modeling for laser drilling process—i. mathematical modeling and numerical methodology. *International Journal of Heat and Mass Transfer*, *40*(14), 3351–3360.

Ganesh, R., Faghri, A., & Hahn, Y. (1997b). A generalized thermal modeling for laser drilling process—II. numerical simulation and results. *International Journal of Heat and Mass Transfer*, *40*(14), 3361–3373.

Gerace, S., Divo, E., & Kassab, A. (2006). A localized radial-basis-function meshless method approach to axisymmetric thermo-elasticity. In *9th AIAA/ASME joint thermophysics and heat transfer conference* (June, pp. 1–15). American Institute of Aeronautics and Astronautics (AIAA).

Gingold, R. A. & Monaghan, J. J. (1977). Smoothed particle hydrodynamics: Theory and application to non-spherical stars. *Monthly Notices of the Royal Astronomical Society*, *181*(3), 375–389.

Gower, M. C. (2000). Industrial applications of laser micromachining. *Opt. Express*, *7*(2), 56.

G.R. Liu, X. C. & Reddy, J. (2002). Buckling of symmetrically laminated composite plates using the element-free galerkin method. *Int. J. Str. Stab. Dyn. 02*(03), 281–294.

Groenenboom, P. H. (2009). Hydrodynamics and fluid-structure interaction by coupled SPH-FE method. *Journal of Hydraulic Research*, *48*(extra), 000.

Harničárová, M., Valíček, J., Öchsner, A., Grznárik, R., Kušnerová, M., Neugebauer, J., & Kozak, D. (2013). Predicting residual and flow stresses from surface topography created by laser cutting technology. *Optics & Laser Technology*, *52*, 21–29.

Harp, W., Dilwith, J., & Tu, J. (2008). Laser ablation using a long-pulsed, high-fluence, CW single-mode fiber laser. *Journal of Materials Processing Technology*, *198*(1-3), 22–30.

Hua Li, S. S. M. (2013, February 22). *Meshless methods and their numerical properties*. CRC PR INC.

Huang, C.-S., Lee, C.-F., & Cheng, A.-D. (2007). Error estimate, optimal shape factor, and high precision computation of multiquadric collocation method. *Engineering Analysis with Boundary Elements*, *31*(7), 614–623.

Iglesias, a. S., Rojas, L. P., & Rodríguez, R. Z. (2004). Simulation of anti-roll tanks and sloshing type problems with smoothed particle hydrodynamics. *Ocean Engineering*, *31*(8-9), 1169–1192.

Ion, J. (2005). *Laser Processing of Engineering Materials: Principles, Procedure and Industrial Application*. Butterworth-Heinemann.

Iurlaro, L., Gherlone, M., & Sciuva, M. D. (2014). Energy based approach for shape parameter selection in radial basis functions collocation method. *Composite Structures*, *107*(2), 70–78.

Jeong, J., Jhon, M., Halow, J., & van Osdol, J. (2003). Smoothed particle hydrodynamics: Applications to heat conduction. *Computer Physics Communications*, *153*(1), 71–84.

Jianming, W., Na, G., & Wenjun, G. (2010). Abrasive waterjet machining simulation by SPH method. *International Journal of Advanced Manufacturing Technology*, *50*(1-4), 227–234.

Kansa, E. (1990a). Multiquadrics—a scattered data approximation scheme with applications to computational fluid-dynamics—i surface approximations and partial derivative estimates. *Computers & Mathematics with applications*, *19*(8), 127–145.

Kansa, E. (1990b). Multiquadrics—a scattered data approximation scheme with applications to computational fluid-dynamics—ii solutions to parabolic, hyperbolic and elliptic partial differential equations. *Computers & Mathematics with Applications*, *19*(8), 147–161.

Kao, H.-M. & Chang, T.-J. (2012). Numerical modeling of dambreak-induced flood and inundation using smoothed particle hydrodynamics. *Journal of Hydrology*, *448-449*, 232–244.

Kar, A., Rockstroh, T., & Mazumder, J. (1992). Two-dimensional model for laser-induced materials damage: Effects of assist gas and multiple reflections inside the cavity. *Journal of Applied Physics*, *71*(6), 2560–2569.

Kim, M. J. (2011). Meshfree isoparametric point interpolation method (ipim) for evaporative laser drilling. *Applied Mathematical Modelling*, *35*(6), 2639–2649.

Kim, M. J. (2012). Meshfree isoparametric finite point interpolation method (ifpim) with weak and strong forms for evaporative laser drilling. *Applied Mathematical Modelling*, *36*(4), 1615–1625.

Kim, M. J. (2005). 3D finite element analysis of evaporative laser cutting. *Applied Mathematical Modelling*, *29*(10), 938–954.

Kim, M. J. & Zhang, J. (2001). Finite element analysis of evaporative cutting with a moving high energy pulsed laser. *Applied Mathematical Modelling*, *25*(3), 203–220.

Lancaster, P. & Salkauskas, K. (1981). Surfaces generated by moving least squares methods. *Mathematics of Computation*, *37*(155), 141–158.

Lancaster, P. & estutis Šalkauskas, K. (1986). Curve and surface fitting : An introduction. *London: Academic Press, 1986*, *1*.

Li, K. & Sheng, P. (1995). Plane stress model for fracture of ceramics during laser cutting. *International Journal of Machine Tools and Manufacture*, *35*(11), 1493–1506.

Li, Q.-H., Chen, S.-S., & Kou, G.-X. (2011). Transient heat conduction analysis using the MLPG method and modified precise time step integration method. *Journal of Computational Physics*, *230*(7), 2736–2750.

Li, S. & Liu, W. K. (2002). Meshfree and particle methods and their applications. *Applied Mechanics Reviews*, *55*(1), 1.

Liang, Y., Sun, Z., Xi, G., & Liu, L. (2015). Numerical models for heat conduction and natural convection with symmetry boundary condition based on particle method. *International Journal of Heat and Mass Transfer*, *88*, 433–444.

Limido, J. & Espinosa, C. (2006). A new approach of high speed cutting modelling: SPH method. *Journal de Physique …*, *134*, 1195–1200.

Limido, J., Espinosa, C., Salaün, M., & Lacome, J. L. (2007). SPH method applied to high speed cutting modelling. *International Journal of Mechanical Sciences*, *49*(7), 898–908.

Limido, J., Espinosa, C., Salaun, M., Mabru, C., Chieragatti, R., & Lacome, J. (2011). Metal cutting modelling SPH approach. *International Journal of Machining and Machinability of Materials*, *9*(3/4), 177.

Liszka, T. & Orkisz, J. (1980). The finite difference method at arbitrary irregular grids and its application in applied mechanics. *Computers & Structures*, *11*(1-2), 83–95.

Liu, G. R. & Gu, Y. T. (2005). *An introduction to meshfree methods and their programming*. An Introduction to Meshfree Methods and Their Programming. Berlin/Heidelberg: Springer Science + Business Media.

Liu, G. R., Zhang, G. Y., Gu, Y. T., & Wang, Y. Y. (2005a). A meshfree radial point interpolation method (RPIM) for three-dimensional solids. *Computational Mechanics*, *36*(6), 421–430.

Liu, G.-R. (2009, September 22). *Mesh free methods*. Taylor & Francis Inc.

Liu, Y., Zhang, X., & Lu, M.-W. (2005b). A MESHLESS METHOD BASED ON LEAST-SQUARES APPROACH FOR STEADY- AND UNSTEADY-STATE HEAT CONDUCTION PROBLEMS. *Numerical Heat Transfer, Part B: Fundamentals*, *47*(3), 257–275.

Low, D. K. Y., Li, L., & Byrd, P. J. (2002). Hydrodynamic physical modeling of laser drilling. *Journal of Manufacturing Science and Engineering*, *124*(4), 852.

Lu, Y., Belytschko, T., & Gu, L. (1994). A new implementation of the element free galerkin method. *Computer Methods in Applied Mechanics and Engineering*, *113*(3-4), 397–414.

Lucy, L. B. (1977). A numerical approach to the testing of the fission hypothesis. *The Astronomical Journal*, *82*, 1013.

Maiman, T. H. (1960). Stimulated optical radiation in ruby. *Nature*, *187*(4736), 493–494.

Mavrič, B. & Šarler, B. (2015). Local radial basis function collocation method for linear thermoelasticity in two dimensions. *International Journal of Numerical Methods for Heat & Fluid Flow*, *25*(6), 1488–1510.

Meijer, J. (2004). Laser beam machining (LBM), state of the art and new opportunities. *Journal of Materials Processing Technology*, *149*(1-3), 2–17.

Mirzaei, D. & Schaback, R. (2013). Solving heat conduction problems by the direct meshless local petrov-galerkin (DMLPG) method. *Numerical Algorithms*, *65*(2), 275–291.

Modest, M. F. (1996). Three-dimensional, transient model for laser machining of ablating/decomposing materials. *International Journal of Heat and Mass Transfer*, *39*(2), 221–234.

Monaghan, J. J. (2005). Smoothed particle hydrodynamics. *Reports on Progress in Physics*, *68*(8), 1703–1759.

Mugan, A. K. A. (2012). Solutions of two-dimensional heat transfer problems by using symmetric smoothed particle hydrodynamics method. *Journal of Applied & Computational Mathematics*, *01*(04), 10–15.

Muhammad, N., Rogers, B. D., & Li, L. (2013). Understanding the behaviour of pulsed laser dry and wet micromachining processes by multi-phase smoothed particle hydrodynamics (sph) modelling. *Journal of Physics D-Applied Physics*, *46*(9), 095101.

Ng, G., Crouse, P., & Li, L. (2006). An analytical model for laser drilling incorporating effects of exothermic reaction, pulse width and hole geometry. *International Journal of Heat and Mass Transfer*, *49*(7-8), 1358–1374.

Nguyen, V. P., Rabczuk, T., Bordas, S., & Duflot, M. (2008). Meshless methods: A review and computer implementation aspects. *Mathematics and Computers in Simulation*, *79*(3), 763–813.

Niraula, P., Han, Y., & Wang, J. (2015). Comparison of meshfree and mesh-based methods for boundary value problems in physics. *J. Phys.: Conf. Ser. 640*, 012067.

Oñate, E., Idelsohn, S., Zienkiewicz, O. C., & Taylor, R. L. (1996). A FINITE POINT METHOD IN COMPUTATIONAL MECHANICS. APPLICATIONS TO CONVECTIVE TRANSPORT AND FLUID FLOW. *International Journal for Numerical Methods in Engineering*, *39*(22), 3839–3866.

Paek, U. & Gagliano, F. (1971). Thermal analysis of laser drilling processes. *IEEE Journal of Quantum Electronics*, *7*(6), 277–277.

Pastras, G., Fysikopoulos, A., Stavropoulos, P., & Chryssolouris, G. (2014). An approach to modelling evaporation pulsed laser drilling and its energy efficiency. *The International Journal of Advanced Manufacturing Technology*, *72*(9-12), 1227–1241.

Patel, R. S. & Brewster, M. Q. (1991a). Gas-assisted laser-metal drilling - experimental results. *Journal of Thermophysics and Heat Transfer*, *5*(1), 26–31.

Patel, R. S. & Brewster, M. Q. (1991b). Gas-assisted laser-metal drilling - theoretical model. *Journal of Thermophysics and Heat Transfer*, *5*(1), 32–39.

Qian, L. F. & Batra, R. C. (2004). Three-dimensional transient heat conduction in a functionally graded thick plate with a higher-order plate theory and a meshless local petrov-galerkin method. *Computational Mechanics*, *35*(3), 214–226.

Rabczuk, T., Xiao, S. P., & Sauer, M. (2006). Coupling of mesh-free methods with finite elements: Basic concepts and test results. *Communications in Numerical Methods in Engineering*, *22*(10), 1031–1065.

Razavitoosi, S. L., Ayyoubzadeh, S. A., & Valizadeh, A. (2014). Two-phase SPH modelling of waves caused by dam break over a movable bed. *International Journal of Sediment Research*, *29*(3), 344–356.

Rosswog, S. (2009). Astrophysical smooth particle hydrodynamics. Elsevier BV. arXiv: 0903.5075

Salonitis, K., Stournaras, A., Tsoukantas, G., Stavropoulos, P., & Chryssolouris, G. (2007). A theoretical and experimental investigation on limitations of pulsed laser drilling. *Journal of Materials Processing Technology*, *183*(1), 96–103.

Schulz, W., Eppelt, U., & Poprawe, R. (2013). Review on laser drilling i. fundamentals, modeling, and simulation. *Journal of Laser Applications*, *25*(1), 012006.

Semak, V. V., Damkroger, B., & Kempka, S. (1999). Temporal evolution of the temperature field in the beam interaction zone during laser material processing. *Journal of Physics D: Applied Physics*, *32*(15), 1819–1825.

Semak, V. V. & Miller, T. F. (2013). Simulation of laser penetration efficiency. *Journal of Physics D: Applied Physics*, *46*(38), 385501.

Semak, V. & Matsunawa, A. (1997). The role of recoil pressure in energy balance during laser materials processing. *Journal of Physics D: Applied Physics*, *30*(18), 2541–2552.

Shao, J., Li, H., Liu, G., & Liu, M. (2012). An improved SPH method for modeling liquid sloshing dynamics. *Computers & Structures*, *100-101*, 18–26.

Shaofan Li, W. K. L. (2007, March 7). *Meshfree particle methods*. Springer.

Shen, Z., Zhang, S., Lu, J., & Ni, X. (2001). Mathematical modeling of laser induced heating and melting in solids. *Optics & Laser Technology*, *33*(8), 533–537.

Shidfar, A., Alinejadmofrad, M., & Garshasbi, M. (2009). A numerical procedure for estimation of the melt depth in laser material processing. *Optics & Laser Technology*, *41*(3), 280–284.

Singh, I. V. (2005). Heat transfer analysis of composite slabs using meshless element free galerkin method. *Computational Mechanics*, *38*(6), 521–532.

Singh, I. (2004). A numerical solution of composite heat transfer problems using meshless method. *International Journal of Heat and Mass Transfer*, *47*(10-11), 2123–2138.

Solana, P., Kapadia, P., Dowden, J. M., & Marsden, P. J. (1999). An analytical model for the laser drilling of metals with absorption within the vapour. *Journal of Physics D: Applied Physics*, *32*(8), 942–952.

Souto-Iglesias, a., Delorme, L., Pérez-Rojas, L., & Abril-Pérez, S. (2006). Liquid moment amplitude assessment in sloshing type problems with smooth particle hydrodynamics. *Ocean Engineering*, *33*(11-12), 1462–1484.

Springel, V. (2010). Smoothed particle hydrodynamics in astrophysics. *Annual Review of Astronomy and Astrophysics*, *48*(1), 391–430. arXiv: 1109.2219

Steen, W. M. & Mazumder, J. (2010). *Laser material processing* (4th). Springer Science + Business Media.

Su, C. S. C., Zhang, Y. Z. Y., Hou, J. H. J., & Wang, W. W. W. (2008). Numerical simulation and analysis for metal cutting processes based on FEM and SPH. In *2008 asia simulation conference - 7th international conference on system simulation and scientific computing* (pp. 1325–1328). IEEE.

Tsai, C. L., Guan, Y. L., Batra, R. C., Ohanehi, D. C., Dillard, J. G., Nicoli, E., & Dillard, D. A. (2012). Comparison of the performance of SSPH and MLS basis functions for two-dimensional linear elastostatics problems including quasistatic crack propagation. *Computational Mechanics*, *51*(1), 19–34.

Veres, I. A., Berer, T., & Burgholzer, P. (2013). Numerical modeling of thermoelastic generation of ultrasound by laser irradiation in the coupled thermoelasticity. *Ultrasonics*, *53*(1), 141–149.

Verhoeven, J., Jansen, J., Mattheij, R., & Smith, W. (2003). Modelling laser induced melting. *Mathematical and Computer Modelling*, *37*(3-4), 419–437.

von Allmen, M. (1976). Laser drilling velocity in metals. *Journal of Applied Physics*, *47*(12), 5460–5463.

Vorobyev, A., Kriventsev, V., & Maschek, W. (2011). Simulation of central sloshing experiments with smoothed particle hydrodynamics (SPH) method. *Nuclear Engineering and Design*, *241*(8), 3086–3096.

Vuyst, T. D., Vignjevic, R., & Campbell, J. (2005). Coupling between meshless and finite element methods. *International Journal of Impact Engineering*, *31*(8), 1054–1064.

Wang, Y.-F. & Yang, Z.-G. (2009). A coupled finite element and meshfree analysis of erosive wear. *Tribology International*, *42*(2), 373–377.

Wang, J. G. & Liu, G. R. (2002a). A point interpolation meshless method based on radial basis functions. *International Journal for Numerical Methods in Engineering*, *54*(11), 1623–1648.

Wang, J. & Liu, G. (2002b). On the optimal shape parameters of radial basis functions used for 2-D meshless methods. *Computer Methods in Applied Mechanics and Engineering*, *191*(23-24), 2611–2630.

Wang, Z.-B., Chen, R., Wang, H., Liao, Q., Zhu, X., & Li, S.-Z. (2016). An overview of smoothed particle hydrodynamics for simulating multiphase flow. *Applied Mathematical Modelling*, *40*(23-24), 9625–9655.

Wertz, J., Kansa, E., & Ling, L. (2006). The role of the multiquadric shape parameters in solving elliptic partial differential equations. *Computers & Mathematics with Applications*, *51*(8), 1335–1348.

Wu, X., Shen, S., & Tao, W. (2007). Meshless local petrov-galerkin collocation method for two-dimensional heat conduction problems. *Computer Modeling in Engineering and Sciences*, *22*(1), 65.

Wu, X.-H. & Tao, W.-Q. (2008). Meshless method based on the local weak-forms for steady-state heat conduction problems. *International Journal of Heat and Mass Transfer*, *51*(11-12), 3103–3112.

Xie, J., Kar, A., Rothenflue, J. A., & Latham, W. P. (1997). Comparative studies of metal cutting with high-power lasers. In *XI international symposium on gas flow and chemical lasers and high-power laser conference* (p. 764). SPIE-Intl Soc Optical Eng.

Xiong, H.-b. & Zhu, J. (2010). Study of droplet deformation, heat-conduction and solidification using incompressible smoothed particle hydrodynamics method. *Journal of Hydrodynamics*, *22*(5), 150–153.

Yang, Y., Chen, Z., & Zhang, Y. (2016). Melt flow and heat transfer in laser drilling. *International Journal of Thermal Sciences*, *107*, 141–152.

Yeo, C., Tam, S., Jana, S., & Lau, M. W. (1994). A technical review of the laser drilling of aerospace materials. *Journal of Materials Processing Technology*, *42*(1), 15–49.

Yilbas, B. S. & Naqvi, I. Z. (2003). Laser heating including the phase change process and thermal stress generation in relation to drilling. *Proceedings of the Institution of Mechanical Engineers, Part B: Journal of Engineering Manufacture*, *217*(7), 977–991.

Zahedi, A., Li, S., Roy, A., Babitsky, V., & Silberschmidt, V. V. (2012). Application of smooth-particle hydrodynamics in metal machining. *Journal of Physics: Conference Series*, *382*, 012017.

Zhang, G. M. & Batra, R. C. (2008). Symmetric smoothed particle hydrodynamics (SSPH) method and its application to elastic problems. *Computational Mechanics*, *43*(3), 321–340.

Zhang, M. Y., Zhang, H., & Zheng, L. L. (2008). Simulation of droplet spreading, splashing and solidification using smoothed particle hydrodynamics method. *International Journal of Heat and Mass Transfer*, *51*(13-14), 3410–3419.

Zhang, W., Yao, Y., & Chen, K. (2001). Modelling and analysis of UV laser micromachining of copper. *The International Journal of Advanced Manufacturing Technology*, *18*(5), 323–331.

Zhang, X., Song, K. Z., Lu, M. W., & Liu, X. (2000). Meshless methods based on collocation with radial basis functions. *Computational Mechanics*, *26*(4), 333–343.

Zhang, X. H., Ouyang, J., & Zhang, L. (2009). Matrix free meshless method for transient heat conduction problems. *International Journal of Heat and Mass Transfer*, *52*(7-8), 2161–2165.

Zhang, X. & Xiang, H. (2015). A fast meshless method based on proper orthogonal decomposition for the transient heat conduction problems. *International Journal of Heat and Mass Transfer*, *84*, 729–739.

Zhang, Y., Li, S., Chen, G., & Mazumder, J. (2013a). Experimental observation and simulation of keyhole dynamics during laser drilling. *Optics & Laser Technology*, *48*, 405–414.

Zhang, Y., Shen, Z., & Ni, X. (2013b). Numerical simulation of melt ejection during the laser drilling process on metal by millisecond pulsed laser. In S. Kaierle, J. Liu, & J. Cao (Eds.), *2nd international symposium on laser interaction with matter (LIMIS 2012)* (Vol. 8796, *Limis 2012*, p. 87962I). SPIE-Intl Soc Optical Eng.

Zhang, Y., Shen, Z., & Ni, X. (2014). Modeling and simulation on long pulse laser drilling processing. *International Journal of Heat and Mass Transfer*, *73*, 429–437.

Zhang, Y. & Faghri, A. (1999). Vaporization, melting and heat conduction in the laser drilling process. *International Journal of Heat and Mass Transfer*, *42*(10), 1775–1790.

Zhang, Z., Qiang, H., & Gao, W. (2011). Coupling of smoothed particle hydrodynamics and finite element method for impact dynamics simulation. *Engineering Structures*, *33*(1), 255–264.

LIST OF PUBLICATIONS

Abidou, D., Yusoff, N., Nazri, N., Awang, M. O., Hassan, M. A., & Sarhan, A. A. (2017b). Numerical simulation of metal removal in laser drilling using radial point interpolation method. *Engineering Analysis with Boundary Elements*, *77*, 89–96

Abidou, D., Yusoff, N., Nazri, N., Awang, M. O., Hassan, M. A., & Sarhan, A. A. (2017c). Numerical simulation of metal removal in laser drilling using symmetric smoothed particle hydrodynamics. *Precision Engineering*

Abidou, D., Sarhan, A. A., Yusoff, N., Nazri, N., Awang, M. O., & Hassan, M. A. (2017a). Numerical simulation of metal removal in laser drilling using meshless local petrov-galerkin collocation method. *Applied Mathematical Modelling*